

The effect of the present-day imbalance on schematic and climate forced simulations of the West Antarctic Ice Sheet collapse

Tim van den Akker¹, William H. Lipscomb², Gunter R. Leguy², Willem Jan van de Berg¹, Roderik S.W. van de Wal^{1,3,4}

¹Institute for Marine and Atmospheric Research Utrecht, Utrecht University, Netherlands

²Climate and Global Dynamics Laboratory, NSF National Center for Atmospheric Research, Boulder, CO, USA

³Department of Physical Geography, Utrecht University, Netherlands

⁴KNMI Royal Netherlands Meteorological Institute, De Bilt, Netherlands

Correspondence to: Tim van den Akker (t.vandenakker@uu.nl)

Abstract

Recent observations reveal that the West Antarctic Ice Sheet is rapidly thinning, particularly at its two largest outlet glaciers, Pine Island Glacier and Thwaites Glacier, while East Antarctica remains relatively stable. Ice sheet model projections over the next few centuries give a mixed picture, some ice sheet models forced by climate models project mass gain by increased surface mass balance, while most models project moderate to severe mass loss by increasing ice discharge. In this study, we explore the effect of present-day ice thickness change rates on forced future simulations of the Antarctic Ice Sheet using the Community Ice Sheet Model (CISM). We start with a series of schematic, uniform ocean temperature perturbations in the Amundsen Sea Embayment (ASE) to probe the sensitivity of the modelled present-day imbalance to ocean warming. We then apply ocean and atmospheric forcing from seven datasets produced by five Earth System Models (ESMs) from the CMIP5 and CMIP6 ensemble to simulate the Antarctic Ice Sheet from 2015 to 2500. The schematic experiments suggest the presence of an ice-dynamical limit, Thwaites Glacier (TG) cannot collapse (i.e. accelerated deglaciation leading to considerable grounded ice mass loss) before ~2100 without more than 2 degrees of schematic, sudden and uniform ocean warming. Meanwhile, the maximum Global Mean Sea Level rise (GMSLR) from the ASE rate during the collapse increases linearly with ocean temperature, indicating that while earlier collapse timing shows diminishing returns, the rate of sea-level rise keeps on intensifying with stronger forcing. The relative importance of including the observed present-day mass loss rates decreases for larger (ocean) warming under climate forcing, and decreases over time. For the East Antarctic Ice Sheet on shorter timescales (until 2100), adding the present-day observed mass change rates doubles its global mean sea level rise contribution. On longer timescales (2100–2500), the effect of the present-day observed mass change rates is smaller. Thinning of the West Antarctic Ice Sheet induced by the present-day imbalance is to a small degree partly compensated by present-day ice sheet thickening of the East Antarctic Ice Sheet over the coming centuries, which persists in our simulations. Moreover, these deviations are overshadowed by the mass losses induced by the projected ocean warming.

32 1 Introduction

33 The latest IPCC estimate of the Antarctic Ice Sheet (AIS) contribution to global mean sea level (GMSL) rise ranges from 0.03
34 m (SSP1-1.9, low end of the likely range) to 0.34 m (SSP5-8.5, high end of the likely range) in 2100 (Fox-Kemper et al.,
35 2021). This is an assessment based on ice sheet models, which simulate the future behavior of the AIS. The uncertainty
36 modelled ice sheet contribution to sea level from the AIS until 2100 is relatively low because the major floating ice shelves
37 keep the grounded ice sheet currently in place (Van De Wal et al., 2022), but increases rapidly after 2100 because non-linear
38 processes could accelerate mass loss significantly (Fox-Kemper et al., 2021; Payne et al., 2021; Deconto et al., 2021). It is
39 argued that the main contributors to Antarctic mass loss uncertainty on the long term (e.g. after 2100) are the choice of ice
40 flow model and the choice of the Earth System Model (ESM) used as ocean and atmospheric forcing (Pattyn and Morlighem,
41 2020; Aschwanden et al., 2021).

42 Both ice flow models and ESMs have grown in number over the past decades. This has increased the capability to quantify the
43 uncertainty related to the choice of the ice sheet model and to the choice of ESM forcing. The Ice Sheet Model Intercomparison
44 for CMIP6 (ISMIP6, Nowicki et al. (2016); (2020)) exemplifies multi-model ensemble simulations of the AIS and state-of-
45 the-art quantification of different sources of uncertainty in sea level rise projections. Seroussi et al. (2023) show that until
46 2100, the choice of ice sheet model (which encompasses all modellers choices made like the momentum balance
47 approximation, resolution, initialization method and parameterizations) is the dominant source of uncertainty of projected
48 GMSL from the AIS, with a growing uncertainty caused by the choice of ESM forcing over time. This study shows large
49 geographic differences: for example, the variance associated with the ice sheet model is large for Thwaites Glacier (TG) and
50 Pine Island Glacier (PIG), which at present-day exhibit the largest ice thinning rates according to recent observations (Smith
51 et al., 2020), and small for the MacAyeal and Whillans glaciers. In a follow-up study, Seroussi et al. (2024) show that the
52 choice of ice flow model remains the largest source of uncertainty until 2300, with ESM forcing as second largest contributor.
53 Among other model differences, a main difference is the method used to simulate the present-day state of the AIS, here
54 referred to as the initialization method.

55 To obtain a good model representation of the present-day configuration of the AIS it is necessary to do a model initialization.
56 In an initialization, modellers often include the observed ice thickness and/or the observed ice surface velocities as target
57 variables for the model to match (Winkelmann et al., 2011; Pollard and Deconto, 2012; Greve and Blatter, 2016; Quiquet et
58 al., 2018; Lipscomb et al., 2019; Berends et al., 2021; Berends et al., 2022).. In these methods, the ice sheet model adjusts
59 model parameters by comparing modelled and observed ice surface velocities while either imposing observed ice thickness
60 (the so-called Data Assimilation method) or by doing a forward run either with historical or with present-day forcing (the spin-
61 up method). This process can lead in some cases to nonzero ice thickness change rates, or drift, when the model is run forward

62 in time, even without external climate forcing. All three studies by Rosier et al. (2021), Bett et al. (2023) and Rosier et al.
63 (2024) state that it is impossible to obtain a perfect fit between observed and modelled ice thickness, ice surface velocities,
64 and mass change rates simultaneously because the three datasets are not mutually consistent (Morlighem et al., 2011).

65

66 To get the modelled ice sheet to exhibit a mass change rate, ideally also close to observations, a historical forcing scenario can
67 be used (Reese et al., 2023; Coulon et al., 2024; Klose et al., 2024). Recently, Van Den Akker et al. (2025b) developed a
68 method to incorporate the observed mass change rates in this spin-up initialization, in such a way that the resulting modelled
69 ice sheet can start future simulations immediately from the observed imbalance. This circumvents the need for a historical
70 simulation and forcing over the near-present period. Van Den Akker et al. (2025b) show that initialization with the present-
71 day observed mass change rates in two ice-sheet models always leads to an unforced collapse (i.e., without additional ocean
72 or atmospheric warming) of the West Antarctic Ice Sheet (WAIS), starting with Thwaites Glacier (TG) and Pine Island Glacier
73 (PIG). The rapid collapse phase typically begins after a period of 500 - 2000 years of slow retreat. However, that study only
74 showed simulations with a sustained present-day climate; it did not investigate how the present-day imbalance affects
75 simulations that include future climate change (hereafter labelled as ‘forcing’).

76

77 In this study, we focus on forced simulations of the Antarctic Ice Sheet, first using schematic ocean warming, and secondly
78 ocean temperature and SMB anomalies from five ESMs from the CMIP5 and CMIP6 ensembles following either the SSP1-
79 2.6, SSP5-8.5, RCP1-26 or the RCP 5-85 scenario. The schematic forcing consists of a targeted (e.g. only at TG and PIG)
80 sudden uniform ocean warming up to 2 degrees. The ESM forcing used in this study has also been used as forcing for the
81 ISMIP6 Antarctic Ice Sheet study in Seroussi et al. (2024). These anomalies serve as input to long-term future simulations
82 from 2015 to 2500, to capture the longer-term effects of climate change on the mass of the ice sheet. We use two initializations
83 of the Antarctic ice sheet to start our future simulations, namely with and without the observed mass change rates. Hence, the
84 latter starts from steady-state. With these simulations we will investigate the importance for the future evolution of the
85 Antarctic Ice Sheet (AIS) of the current imbalance of the AIS compared to projected future changes in ocean temperature and
86 SMB. For example, do they add up linearly, or does the present-day imbalance influence the forced deglaciation of the WAIS?
87 In section 2, we introduce the Community Ice Sheet Model, and we discuss the general initialization procedure and the oceanic
88 and atmospheric ESM forcings used. In section 3, we show the results of the future projections. Section 4 contains the
89 discussion, followed by conclusions in section 5.

90 2 Methods

91 2.1 Community Ice Sheet Model (CISM)

92 The Community Ice Sheet Model (CISM, (Lipscomb et al., 2019; Lipscomb et al., 2021)) is a thermo-mechanical higher-order
93 ice sheet model, which is part of the Community Earth System Model version 2 (CESM2 (Danabasoglu et al., 2020)). Earlier
94 applications of CISM to Antarctic Ice Sheet retreat can be found in Lipscomb et al. (2021); Berdahl et al. (2023); Van Den
95 Akker et al. (2025b); Van Den Akker et al. (2025a). The variables and constants used in the text and equations below are listed
96 in Supplementary Tables S1 and S2.

97
98 We run CISM with a vertically integrated approximation to the momentum balance, the Depth Integrated Viscosity
99 Approximation (DIVA) (Goldberg, 2011; Lipscomb et al., 2019; Robinson et al., 2022):

$$\frac{\partial}{\partial x} \left(2\underline{\eta} H \left(2 \frac{\partial \underline{u}}{\partial x} + \frac{\partial \underline{v}}{\partial y} \right) \right) + \frac{\partial}{\partial y} \left(\underline{\eta} H \left(\frac{\partial \underline{u}}{\partial y} + \frac{\partial \underline{v}}{\partial x} \right) \right) - \tau_{b,x} = \rho_i g H \frac{\partial s}{\partial x} \quad (1.1)$$

$$\frac{\partial}{\partial x} \left(\underline{\eta} H \left(\frac{\partial \underline{u}}{\partial y} + \frac{\partial \underline{v}}{\partial x} \right) \right) + \frac{\partial}{\partial y} \left(2\underline{\eta} H \left(2 \frac{\partial \underline{v}}{\partial y} + \frac{\partial \underline{u}}{\partial x} \right) \right) - \tau_{b,y} = \rho_i g H \frac{\partial s}{\partial y} \quad (1.2)$$

101 In which $\underline{\eta}$ is the depth-averaged viscosity, H the ice thickness, \underline{u} and \underline{v} respectively the depth-averaged ice velocities in the
102 x- and y-direction, ρ_i the density of glacial ice and s the surface height above sea level. Basal friction, which appears as $\tau_{b,x}$
103 and $\tau_{b,y}$ in Eqs. 1.1 and 1.2, can be parameterized in several ways. In this study we use the regularized Coulomb sliding law
104 first suggested by Joughin et al. (2019) and confirmed with laboratory experiments by Zoet and Iverson (2020):

$$\tau_b = \beta u_b = C_c N \left(\frac{u_b}{u_b + u_0} \right)^{\frac{1}{m}} \quad (1.3)$$

105 where C_c is a unitless parameter in the range $[0, 1]$ controlling the strength of the regularized Coulomb sliding, u_b the ice basal
106 velocities and u_0 and m are free parameters. The effective pressure N is estimated according to Leguy et al. (2014) and Leguy
107 et al. (2021), assuming full ocean connectivity and based on the height above floatation of the grounded ice. This implies that
108 the scheme proposed by Leguy et al. (2014) accounts for basal water pressure (which reduces N) only near grounding lines
109 and not in other parts of the ice sheet; thus the effective pressure equals ice overburden for most of the ice sheet. The effective
110 pressure is then calculated by:

$$N = \rho_i g H \left(1 - \frac{H_f}{H}\right)^p \quad (1.4a)$$

111 where the flotation thickness H_f is given by

$$H_f = \left(0, -\frac{\rho_w}{\rho_i} b\right) \quad (1.4b)$$

112 with ρ_i for the density of glacial ice, ρ_w the density of ocean water, g the gravitational acceleration and b the height of the
113 bedrock

114

115 Since C_c is poorly constrained by theoretical considerations and observations, we use it as a spatially variable tuning parameter.

116 We tune the logarithm of C_c using a nudging method (Lipscomb et al., 2021; Pollard and Deconto, 2012):

117

$$\frac{dC_l}{dt} = -\left(\frac{H - H_{obs}}{H_0 \tau}\right) - \frac{2}{H_0} \frac{dH}{dt} - \frac{r}{\tau} (C_l - C_{lr}) + \frac{L^2}{\tau} \Delta C_l \quad (1.5a)$$

118

$$C_l = \log(C_c) \quad (1.5b)$$

119 In 1.5a, H_0 , τ , r and L are scaling constants, used to adjust the relative weights of the different terms. Increasing/decreasing
120 H_0 makes the optimization less/more sensitive to ice thickness errors; increasing/decreasing τ makes the changes in C_l per
121 timestep smaller/larger, increasing/decreasing r draws C_l more/less to the relaxation target C_{lr} ; and increasing/decreasing L
122 results in a smoother/spikier 2D pattern of optimized C_l . Their values were tested and chosen to represent AIS thickness and
123 surface velocities well, with minimal drift. Table S2 shows their values.

124

125 The logarithmic relaxation target C_{lr} is a 2D field that penalizes very high and low values of C_c . It is based on elevation, with
126 lower values at low elevation where soft marine sediments are likely more prevalent, following Winkelmann et al. (2011). We
127 chose targets of 0.1 for bedrock below -700 m asl and 0.4 for 700 m asl, with linear interpolation in between, based on
128 Aschwanden et al. (2013). The motivation for this is that lower elevations deglacierate earlier and therefore have more softer
129 marine till relative to higher elevated bedrock, since they likely were deglacierated more in the past compared to regions with
130 higher bedrock. The parameterization and associated values used to represent marine sediments in Aschwanden et al. (2013),
131 which rely solely on bedrock elevation, are challenged by the more recent findings of Li et al. (2022), who show that the
132 likelihood of marine sediment does not directly correlate with bedrock height. Incorporating the likelihood map of Li et al.
133 (2022) into CISM and analysing the influence of marine sediments on marine-based ice sheets is beyond the scope of this
134 study, but represents a promising direction for future work.

135

136 The last term on the RHS of Eq. (1.5a) is new compared to Lipscomb et al. (2021), Van Den Akker et al. (2025a) and Van Den
 137 Akker et al. (2025b) and is introduced to smooth the pattern of optimized C_c by suppressing large spatial gradients. Smoothing
 138 also reduces the model drift as a local grounding line position can no longer be pinned by one grid box with high basal friction.
 139

140 Basal melt rates (BMR) are calculated using a quadratic relation with a sub-shelf thermal forcing dataset consisting of all
 141 observations over the past decades combined with the climatology made by Jourdain et al. (2020) during the initialization and
 142 the forced simulations:

$$BMR = \gamma_0 \left(\frac{\rho_w c_{pw}}{\rho_i L_f} \right)^2 ([TF_{base} + \delta T, 0])^2 \quad (1.6)$$

143 in which the baseline thermal forcing, TF_{base} , is the difference between the melting point and the ocean temperature at the
 144 base of the modelled ice shelf, and δT a local correction temperature. The thermal forcing is derived from a climatology based
 145 on Southern Ocean observations of the past few decades (Jourdain et al., 2020). This basal melt parameterization was
 146 developed and tested by Jourdain et al. (2020) and Favier et al. (2019) with the purpose of modelling present-day Antarctic
 147 basal melt rates. The quadratic relationship between thermal forcing and basal melt rates reflects a positive feedback. As the
 148 ice shelf melts, freshwater is added to the cavity, which is more buoyant than the saltier ocean water. This causes the sub-shelf
 149 meltwater plume to rise faster, and through erosion and upwelling of new warm ocean water, the basal melt rates will increase.
 150 Eq. (1.6) parameterizes this feedback to a reasonable approximation for present-day basal melt rates, but it is unknown how
 151 well it simulates basal melt rates for several degrees of (future) ocean warming.

152
 153 The basal melt rates are tuned through the local correction temperature δT such that the floating ice thickness matches as
 154 closely as possible the thickness observations of Morlighem et al. (2020) following a similar procedure as for friction (Eq.
 155 1.5):

$$\frac{d(\delta T)}{dt} = T_s \left[\left(\frac{H - H_{obs}}{H_0 \tau} \right) + \frac{2}{H_0} \frac{dH}{dt} \right] + \frac{(T_r - \delta T)}{\tau} + \frac{L^2}{\tau} \Delta \delta T, \quad (1.7)$$

157
 158 in which T_s is the temperature scale of the nudging method (0.5 K in this study). This tuning increases (decreases) the local
 159 correction temperature δT in grid cells where the modelled ice shelf is too thick (thin), increasing (decreasing) the basal melt
 160 rates. The tuning includes a relaxation target T_r , being 0, to penalize large deviations from the dataset of Jourdain et al. (2020).
 161 The melt sensitivity γ_0 is chosen to be 3.0×10^4 m/yr, which was used in Lipscomb et al. (2021); Van Den Akker et al.
 162 (2025b); Van Den Akker et al. (2025a) to obtain basal melt rates in agreement with observations and a shelf average δT close
 163 to zero in the Amundsen Sea Embayment, where currently the largest ice shelf melt rates are observed (Adusumilli et al.,
 164 2020). The last term is added to, just as for the C_c optimization in Eq. (1.5), suppress large spatial variations in the optimized
 165 ocean temperature perturbation field, as large spatial gradients of several degrees between grid cells is physically implausible.

166

167 To prevent abrupt jumps in modeled quantities at the grounding line (such as basal friction and basal melt), we use a
168 grounding line parameterization from Leguy et al. (2021):

$$f_{float} = -b - \frac{\rho_i}{\rho_w} H \quad (1.8)$$

169 When f_{float} is positive it is equal to the distance between the ice shelf base and the ocean floor and hence, the ice is floating.

170 When f_{float} is negative, it can be interpreted as the ice thickness change needed for the ice column to become floating. The
171 variable f_{float} is used to compute the floating fraction as a percentage of grid cell area by bilinearly interpolating its value
172 from cell vertices to the cell areas scaled to the cavity thickness (Leguy et al. (2021)). The grounded and floating fraction of a
173 cell are then used to scale basal friction and basal melting. For the basal melting, this is referred to as the Partial Melt
174 Parameterization (PMP), see Leguy et al. (2021).

175

176 Schematic tests by Seroussi and Morlighem (2018) showed that applying basal melt in proportion to the floating area fraction
177 can lead to an overestimation of grounding line retreat rates; they therefore discouraged the use of PMPs. However, Leguy et
178 al. (2021) conducted similar schematic tests with CISM and found that using a PMP reduced the CISM's sensitivity to grid
179 resolution more than the No-Melt Parameterization (NMP) recommended by Seroussi and Morlighem. In more realistic AIS
180 applications of CISM Lipscomb et al. (2021) found that the PMP produced a moderate sensitivity of grounding line migration
181 rates to grid resolution, lower than the sensitivities to basal melt rate and basal friction parameterizations. These results suggest
182 that the optimal GLP is model-dependent and that for CISM, 4-km grid resolution using a PMP is sufficient for modeling
183 continental-scale ice sheets on multi-century timescales.

184

185 We run CISM on a uniform 4 km grid, justified below. using the grounding line parameterization from Leguy et al. (2021)
186 which scales the basal sliding and melt rate proportionally to its grounded and floating area fraction respectively. Doing so,
187 Leguy et al. (2021) showed that this resolution is adequate to capture grounding line dynamics using CISM and idealized
188 marine ice sheet experiments, Lipscomb et al. (2021) showed that this resolution in combination with the scaling reduces the
189 model result's grid resolution dependency when modelling the AIS.

190

191 There are several calving laws in the literature e.g. Yu et al. (2019); Wilner et al. (2023); Greene et al. (2022) and specifically
192 for Greenland (Choi et al., 2018). However, there is no agreed-upon best approach to Antarctic calving (Levermann et al.,
193 2012), and most calving laws struggle to reproduce the observed calving front at multiple locations simultaneously without
194 adjusting local parameters (Amaral et al., 2020). We therefore choose to apply a simple no-advance calving scheme, preventing
195 the calving front from advancing beyond the observed present-day location. The ice shelf front can retreat only through ice
196 shelf thinning. This implies that the ice shelf front can only retreat when the basal melt rates increase greatly and become
197 sufficiently high to remove floating ice upstream of the present-day calving front. In practice, this means that the calving

198 front will only retreat when the basal melt rates are increased greatly, and for present-day conditions, this means that the
 199 calving front position is fixed at its observed location. This is a conservative approach, ignoring the possibility of calving-front
 200 retreat through shelf thinning or of shelf collapse by hydrofracturing. The implementation of a more physically-based calving
 201 law in CISM is the topic of ongoing research.

202

203 **2.2 Initializations**

204 We perform initializations with or without incorporating the observed present-day mass change rates, hence leading to a
 205 transient and equilibrium initial state, respectively. For the equilibrium initialization, C_c and δT are tuned using Eqs. (1.5) and
 206 (1.7) until the modelled ice sheet is in equilibrium, thus $\partial H/\partial t = 0$, given by

$$\frac{\partial H}{\partial t} = -\nabla(\underline{u}H) + B \quad (1.9)$$

207 In Eq. (1.8), \underline{u} is the vertical mean velocity, and B the sum of the basal and SMBs. For the transient initialization, C_c and δT
 208 are tuned using mass conservation complemented by the present-day observed mass change rates as was done by Van Den
 209 Akker et al. (2025b), using

210

$$\frac{\partial H}{\partial t} = -\nabla(\bar{u}H) + B - \left. \frac{\partial H}{\partial t} \right|_{obs} \quad (1.10)$$

211 in which the last term, the pseudo-flux, is the observed mass change from Smith et al. (2020). By subtracting this observed
 212 mass change, mass is added during the initialization where thinning is observed. After the initialization and for normal forward
 213 simulations, this pseudo-flux is removed, so that model simulations start with an imbalance and a thinning rate closely
 214 matching the observed thinning rates. Both initializations are run for 10 kyr, which proved to be long enough to reach a
 215 (thermal) equilibrium. We evaluate both initializations by comparing to observations of ice thickness (Morlighem et al., 2020),
 216 ice surface velocities (Rignot et al., 2011), total basal melt fluxes (Adusumilli et al., 2020; Rignot et al., 2013) and by evaluating
 217 their model drift. We test the drift by running forward for 1000 years (i.e., to the year 3015) without additional forcing with
 218 respect to present-day conditions, with the optimized parameters (e.g. δT and C_c in Eqs. (1.5) and (1.7) kept constant, and with
 219 continuing adding the observed mass changes for the transiently initiated model state as described by Eq. (1.10). This is a time
 220 scale longer than our period of interest, which runs only to 2500, thus for 485 years. The resulting drift, shown in Figures S1
 221 and S2, results in a WAIS change in IVAF over 1000 years of 0.5% for the Transient initialization and approximately 0% for
 222 the equilibrium initialization. For the whole AIS, the model drift in the transient initialization is 0.05% of the IVAF and -
 223 0.05% for the equilibrium initialization. These results ensure that we can attribute any major changes in ice sheet mass to the
 224 applied forcing and not to model drift. Figure S3 shows the evolution of the average temperature during the initialization: it
 225 flattens out at 10 kyr, indicating that the ice sheet has reached thermal equilibrium.

226

227 **2.3 Idealized schematic warming scenarios**

228

229 To assess how sensitive the simulations starting from the transient initialization are to imposed ocean warming, and to compare
230 this with the sensitivity of simulations starting from the equilibrium initialization, we conduct a set of idealized experiments
231 in which ocean temperatures in the ASE region are systematically increased after initialization. Each experiment is then run
232 for 1000 years to allow for a possible WAIS collapse. Ocean temperatures are incremented from 0 K to 2 K in 0.2 K steps,
233 yielding ten simulations for each initialization

234

235 **2.4 ESM forced Future projections**

236 We first test the sensitivity of the two initializations to schematic and sudden ocean warming by conducting 11 idealized
237 experiments with sudden and sustained warming, only in the ASE region shown in Figure S3. We raise the ocean temperatures
238 in these schematic tests, which appears as the sum $TF_{base} + \delta T$ in Eq. (1.6), from 0 to 2 K with steps of 0.2 K.

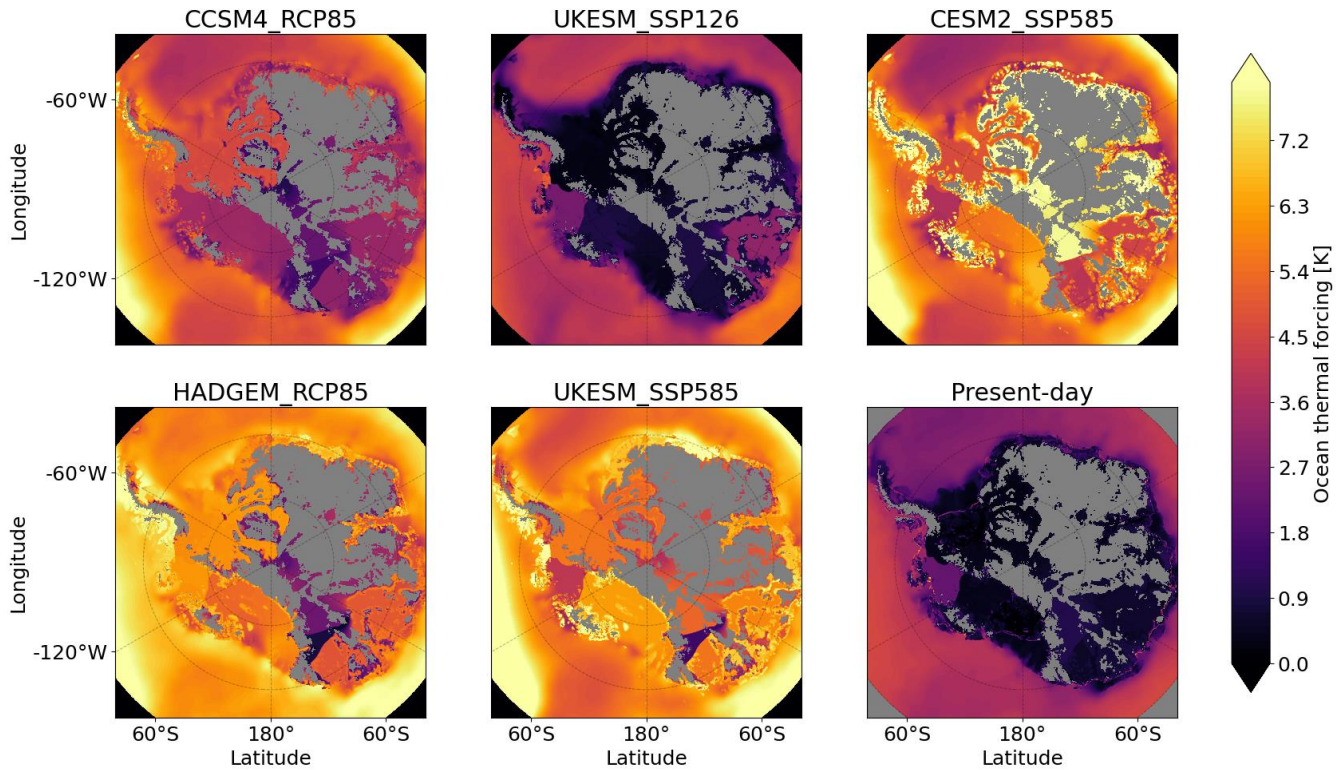
239

240 We then perform two sets (i.e. starting from the transient and starting from the equilibrium initialization) of simulations for
241 each of the seven forcing datasets produced by the five different ESMs, introduced in the next section. We timestamp the end
242 of our initialization at 2015 based on the observational datasets used to calibrate the model (Smith et al., 2020; Morlighem et
243 al., 2020; Rignot et al., 2011). We then run CISM forward for 485 years to 2500. The seven forcing datasets from five different
244 ESMs span the period 1995–2100, with four ESMs continuing until 2300 and one where the input forcing to the ESM was
245 repeated from the late 21st century onwards. For the last 200 years of the simulations, we fix the thermal forcing and SMB
246 anomalies at the last datapoint year being 2300. We consider the whole continent in our analysis, but focus on areas with large
247 changes and potentially large sea level contributions, like the Amundsen Sea Embayment, the Filchner-Ronne basin, and the
248 Ross basin. Those areas are shown in Figure S3.

249

250 We use the same set of ocean and SMB forcings as Seroussi et al. (2024). The ocean and SMB forcings stem from seven ESM
251 simulations from the CMIP5 and CMIP6 ensemble. Two models from the CMIP5 ensemble were selected by Barthel et al.
252 (2020): the Community Climate Model (CCSM4) and the Hadley Centre Global Environment Model (HadGEM2-ES), with
253 respective Equilibrium Climate Sensitivities (ECS) of 2.9 and 4.6 (Meehl et al., 2020). Additionally, two CMIP6 participating
254 models are used: the Community Earth System Model (CESM2) and the UK Earth System Model (UKESM), with ECS of
255 respectively 5.2 and 5.3 (Meehl et al., 2020). The Norwegian Earth System Model (NorESM, ECS of 2.5 as reported by Meehl
256 et al. (2020)) was used as a reference run in the ISMIP6 ensemble and will be used in this study as well. The models
257 HADGEM2-ES, CESM2 and UKESM have a climate sensitivity to doubling of CO₂ concentrations at the upper end of the
258 90% confidence interval in the IPCC-AR6 report (Meehl et al., 2020). More information on the selection of these ESM forcings
259 can be found in Barthel et al. (2020) and Seroussi et al. (2024).

260



262

263 **Figure 1. Thermal forcing ($TF_{base} + \delta T$ in Eq. (1.6)) from the five ESMs used.** Thermal forcing averages for the year 2300 (except the
 264 present-day) are shown for a depth of -500 metres. Cells with bedrock above sea level are shown in grey. The simulations from NorESM
 265 run until 2100 and are shown in Figure S

266

267 The ocean forcings from the ESMs are applied similar to the thermal forcing TF_{base} in Eq. (1.6). For this set of simulations,
 268 cavity- resolving ocean models were not available among the CMIP5 and CMIP6 ensembles. Therefore, the ocean thermal
 269 forcing from the ESMs is interpolated into the ice shelf cavities by Jourdain et al. (2020). First, a marine connection mask is
 270 generated, marking cells with subzero topographic paths to the open ocean. Next, empty cells adjacent to filled ones and
 271 connected to the ocean are identified, following Jourdain et al. (2020). These cells are then filled with the average of
 272 neighboring filled values. Any empty cells below the new fill may remain if the local bedrock is deeper than in adjacent
 273 columns. In those cases, the thermal forcing is linearly extrapolated using a depth-dependent freezing point correction with a
 274 temperature coefficient of $7.64 \times 10^{-4} \text{ K m}^{-1}$ from Beckmann and Goosse (2003). The The last year 2300 of all 7 oceanic
 275 forcings, including the extrapolation below present-day grounded ice, relative to TF_{base} , are shown in Figure 1.

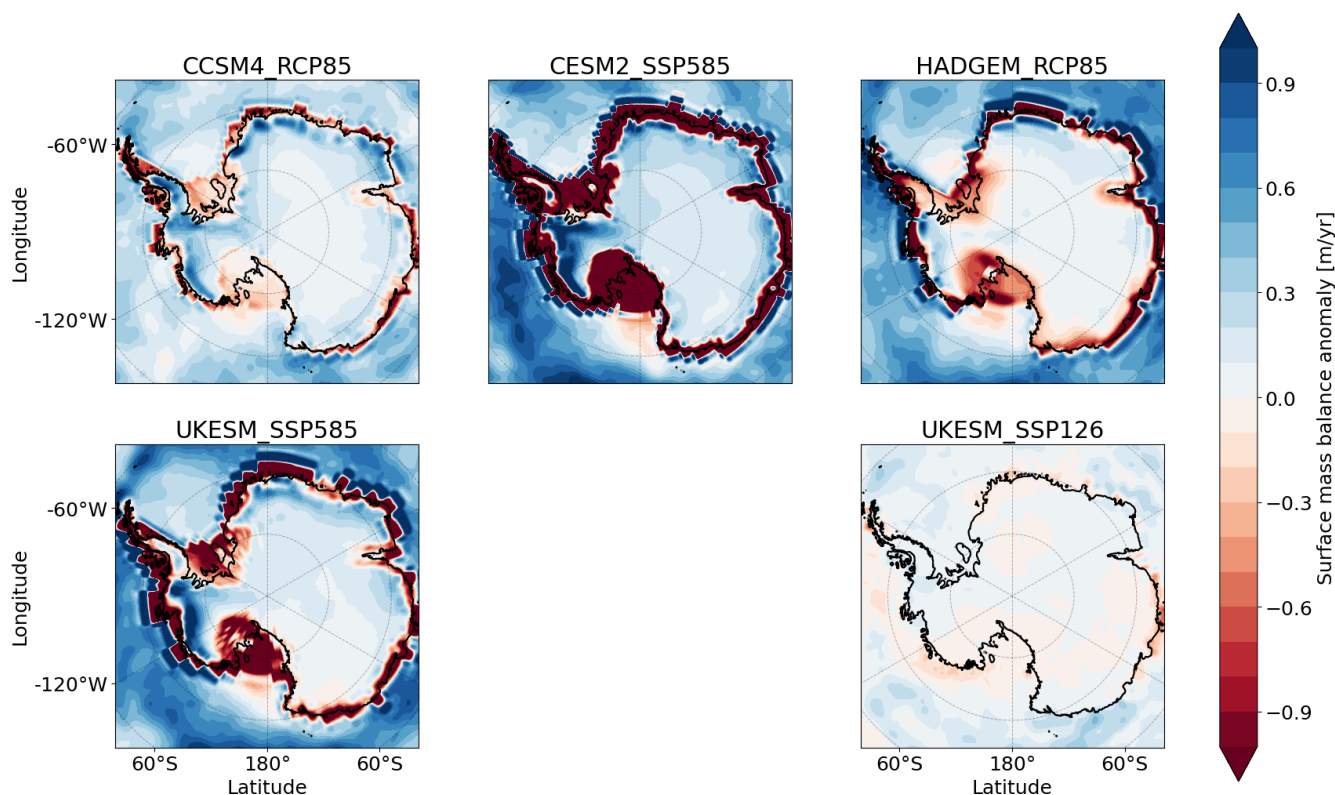
276

277 The computed ocean thermal forcing dataset has 30 layers with a vertical resolution of 60 metres and extends down to 1770 m
 278 below sea level. The thermal forcing at the ice-shelf base is linearly interpolated between vertically adjacent ocean layers. If

279 the ice lies below the lowest ocean layer, which can occur in deep troughs beneath the Filchner-Ronne and Amery shelves, the
280 thermal forcing is extrapolated from the lowest layer using the depth-dependent freezing point temperature coefficient from
281 Beckmann and Goosse (2003).

282
283 Figure 2 shows the SMB anomalies of seven simulations of the five ESMs. Large differences in magnitude are visible, with
284 NorESM_RCP26 and NorESM_RCP85 having hardly any change in SMB compared to present day. On the other hand,
285 CESM2_SSP585 and UKESM_SSP585 show large areas where the SMB decreases considerably due to surface melt. For
286 many of these areas the local SMB becomes net negative, which does occur at present at very few locations only (Mottram et
287 al., 2021; Van Wessem et al., 2018). The simulations that show considerable SMB reduction by surface melt over the ice
288 shelves (CCSM4_RCP85, CESM2_SSP585, HADGEM_RCP85 and UKESM_SSP585) also project an increasing SMB in the
289 course of time for the WAIS ice divide and in Dronning Maud Land. The latter location currently shows thickening as well
290 (Smith et al., 2020).

291



292

293

294 **Figure 2. Surface mass balance (SMB) anomalies simulated by the five ESMs.** The last year of the original datasets, which is 2300 for
295 all simulations except the NorESM simulations, which end in 2100) is shown. Anomalies are added directly to the modelled present-day

296 SMB from RACMO (Van Wessem et al., 2018) annually in the continuation simulations. The observed grounding line position is shown in
297 black.

298 Four of the ESMs (CESM4, HadGEN2-ES, CESM2 and UKESM) were run forward from the historical period until 2300,
299 with high emissions continuing long after 2100 in the high-emission scenarios (RCP85 and SSP5-8.5). For these models, we
300 fix the thermal forcing and SMB anomalies at the 2300 values during the last 200 years of the simulation. NorESM,
301 however, was run only until 2100. After 2100, the NorESM forcing in our simulations is held fixed at late 21st century
302 values. Thus, the NorESM forcing is not directly comparable to the other ESMs after 2100.

303

304 **3. Results**

305 **3.1 Initialization evaluation**

306 Figures 3 - 5 presents the key performance metrics for the equilibrium and transient initializations, namely the difference
307 between observed and modelled ice thickness, surface ice velocities and mass change rates. Supplementary Figures S4 and S5
308 show the spatial patterns of the ice thickness and surface velocity errors with respect to observations, and the optimized
309 quantities for both initializations.

310

311 Overall ice thickness biases are low (Fig 3), especially compared to the velocity errors. In both initializations, we tune towards
312 an observed ice thickness target and not to an ice surface velocity target. The velocity biases are relatively high, but still of the
313 same order of magnitude as many ISMIP6 models (see Seroussi et al. (2020)). Including the present-day mass change rates
314 increases the ice thickness and ice velocity RMSE slightly. Furthermore, in areas where large thinning rates are observed, such
315 as PIG and TG, the dynamic imbalance pseudo-flux in Eq. (1.9) adds considerable mass during the spin-up, which brings the
316 modelled ice fluxes across the grounding line in the transient initialization more in line with observations than in the
317 equilibrium initialization, similarly to as discussed by Van Den Akker et al. (2025b); Van Den Akker et al. (2025a). Using the
318 same flux gates and calculation as Van Den Akker et al. (2025b), the observed ice fluxes in this study are at PIG and TG are
319 31.1 km² yr⁻¹ and 26.1 km² yr⁻¹, respectively. In the equilibrium initialization, those fluxes are 17.0 km² yr⁻¹ and 17.4 km²
320 yr⁻¹, hence much lower than observed. Using the present-day mass change rates and the initialization as described in Section
321 2 results in PIG and TG fluxes of 30.4 km² yr⁻¹ and 24.5 km² yr⁻¹, which are in good agreement with observations.

322

323 In areas with observed thickening in the dataset of Smith et al. (2020), such as at the EAIS, the sum of all ice fluxes including
324 the pseudo-flux in Eq. (1.10) can become of similar or larger magnitude as the negative of the SMB. This requires for these
325 locations, for an equilibrated transient ice sheet, a largely reduced ice flux divergence or even ice flux convergence compared
326 to the equilibrated equilibrium ice sheet. Since ice velocities are low at these locations, and therefore the ice flux is small, the
327 basal friction cannot always decrease the ice velocity enough to reach a steady state with the correct ice thickness, and hence

328 the ice sheet thins locally until a new equilibrium is reached. Consequently, adding the observed present-day mass change
329 rates in these locations yields a negative modelled ice thickness bias, visible on the EAIS in Figure S2. This increases the
330 RMSE of the modelled ice thickness with respect to observations.

331

332 The ice surface velocity biases are generally low in both initializations, except for the Siple coast glaciers and the Ronne ice
333 shelf. Regarding the Siple Coast, the thickness biases are low, indicating that the friction constant optimization in these spots
334 can nudge the modelled ice thickness close to observations, typically with a low C_c in the ice streams. This apparently leads to
335 an overestimation of the ice surface velocity in these ice streams, which can be counteracted by locally tuning parameters
336 related directly to the ice velocities, like the viscosity or the flow enhancement factor. However, the relative error in these ice
337 streams, where the ice surface velocities exceed 2 km yr^{-1} , is still small.

338

339 The same holds for the Ronne shelf, where the modelled ice surface velocities are too low. The ice thickness error at the
340 Filchner-Ronne shelf in both initializations is low, again indicating that the nudging of δT is capable in reproducing the
341 observed ice thicknesses. However, the nudging of δT does not alter the modelled ice thickness by changing the ice velocities
342 as it does for the friction constant optimization. To obtain a better fit, just as with the glaciers at the Siple Coast, parameters
343 directly related to the ice velocities can be nudged. This decreases the misfit between modelled and observed ice surface
344 velocities as shown by Van Den Akker et al. (2025a), but it also introduces another time-constant but spatially varying
345 parameter with associated uncertainties and the risk of over-tuning.

346

347 Figure 5 shows the binned mass change rates from the observations and both model initializations. The transient
348 initialization reproduces the observed thinning rates almost perfectly. For positive rates, the modeled values begin to diverge
349 from the observations in grounded regions where observed thickening exceeds 0.5 m yr^{-1} , which occurs in less than 0.01 %
350 of the modeled grid cells. This discrepancy arises because the model can no longer reduce ice flux by increasing friction; C_c
351 in Eq. 1.4 has reached its upper limit of 1. The surface mass balance and ice inflow into the cell become insufficient to
352 reproduce the observed mass change. These cases of underestimated ice sheet thickening occur mainly in the interior of the
353 EAIS, a region with little to no dynamic connection to the WAIS.

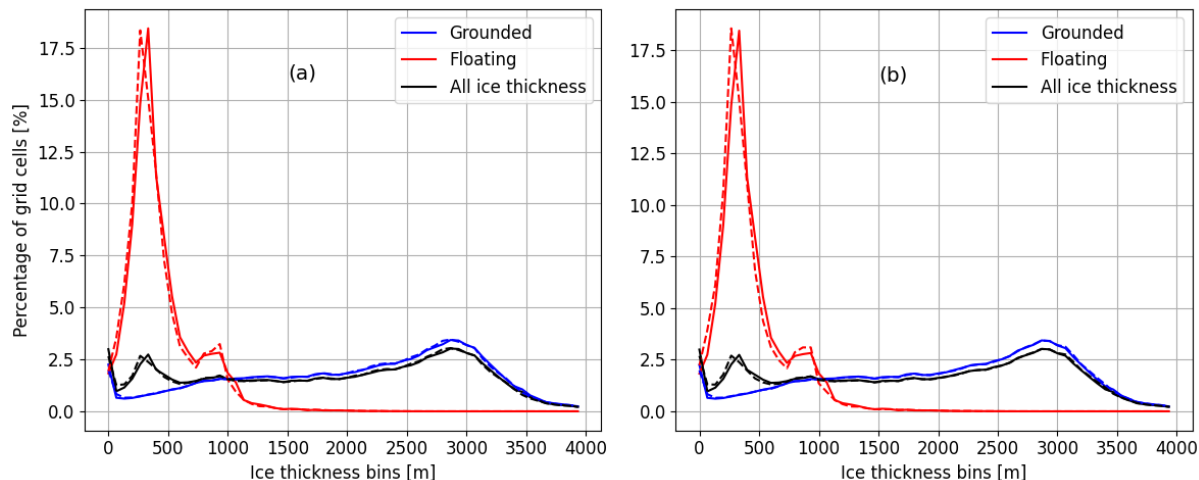
354

355 For floating grid cells, the model cannot reproduce observed thickening rates because ice accretion is not formally
356 represented in the ISMIP6 basal melt parameterization. This restriction arises from the inability to specify where the positive
357 mass change terms Eq. 1.9 should be applied, on top or on the bottom of a floating ice column.

358

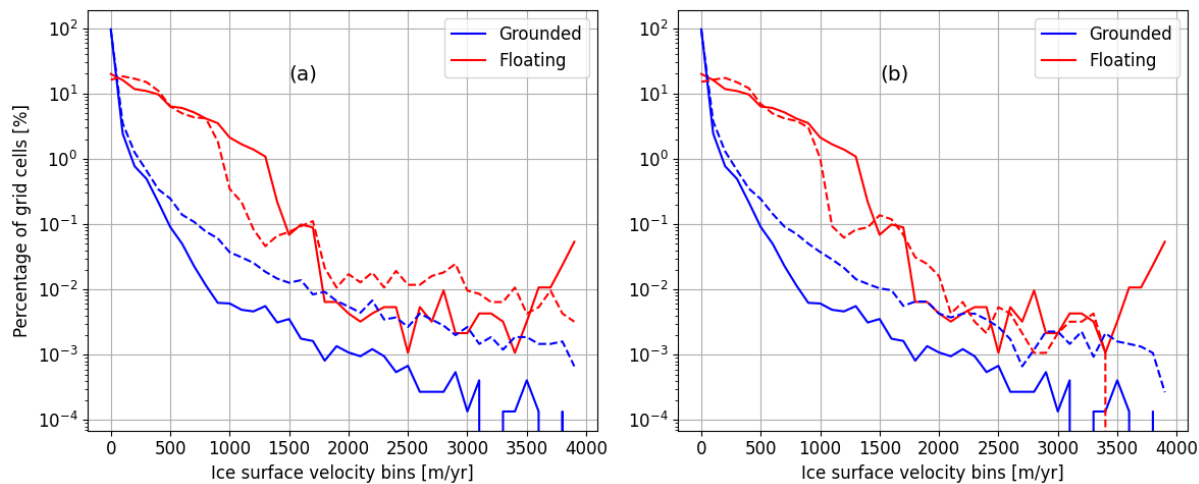
359 The equilibrium simulation presents a different pattern. As expected, it fails to capture the observed present-day mass change
360 rates completely, as it was initialized to be in equilibrium. Consequently, it exhibits minimal model drift, only 0.001 % of the
361 modeled grid cells show a drift greater than 0.1 m yr^{-1} .

362
363
364
365



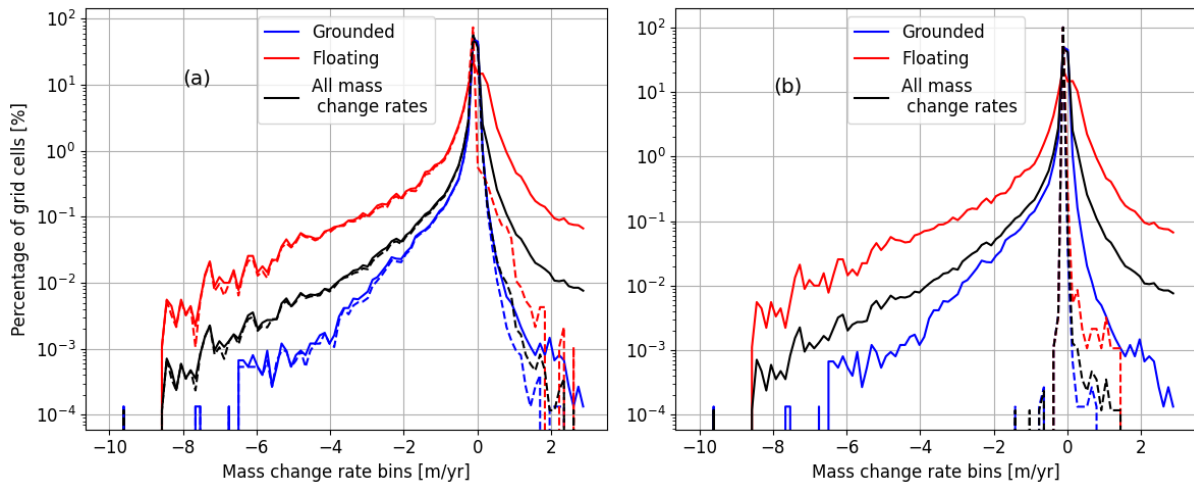
366

367 Figure 3. Binned ice thickness (m) for the observed (solid) and modelled ice (dashed lines). The present-day condition of the
368 transient initialization is shown on the left, the equilibrium simulation on the right. For the transient initialization, the root
369 mean square errors (RMSEs) for floating ice, grounded ice and in total are respectively 44, 31 and 35 meters. For the
370 equilibrium initialization they are respectively 50, 23 and 30 m.



371

372 Figure 4. Binned ice surface velocities (m yr⁻¹) for the observed (solid) and modelled ice (dashed lines). The present-day
373 condition of the transient initialization is shown on the left, the equilibrium simulation on the right. For the transient
374 initialization, the Root Mean Square Errors (RMSEs) for floating ice, grounded ice and in total are respectively 201, 112 and
375 143 m yr⁻¹. For the equilibrium initialization they are respectively 202, 98 and 130 m yr⁻¹.



376

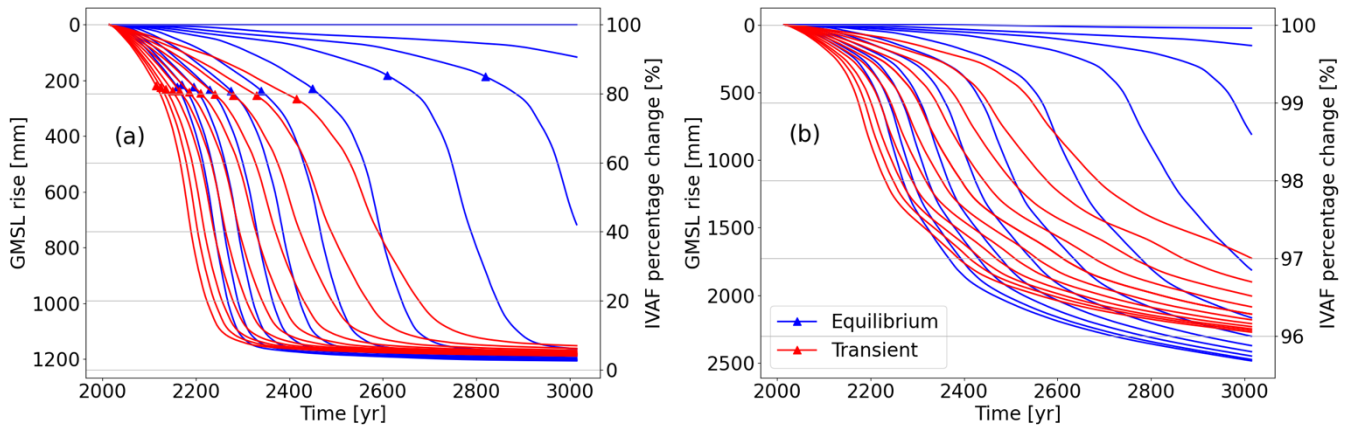
377 Figure 5. Binned mass change rates for the observed ice (solid lines) and the modelled ice (dashed lines). The transient
 378 initialization is shown on the left, and the equilibrium initialization on the right.

379

380 3.2 Schematically forced Antarctic Mass change

381

382



383

384 **Figure 6. Ice Volume Above Floataion response to sudden, uniform ocean warming of the ASE sector, represented as GMSL rise**
 385 **(left y-axis) and as percentage of what was originally present in the ASE region. (a) integrated mass loss in the ASE, where Thwaites**
 386 **Glacier and Pine Island Glacier are situated. Left y-axis shows the GMSL rise in mm and the Ice Volume Above Floataion (IVAF) in**
 387 **percentage of the initial value. (b) The same for the whole AIS. Red lines indicate simulations starting with the observed mass change rates,**
 388 **blue lines indicate simulations starting from an equilibrium. From right to left (later collapse to earlier collapse) the simulations are forced**
 389 **with 0 to 2 K of ocean warming with steps of 0.2 K. Triangles indicate the timestep when the bedrock ridge approximately 50 km inland of**
 390 **the present-day TG grounding line ungrounds, depicted by the line AB in Fig S6.**

391

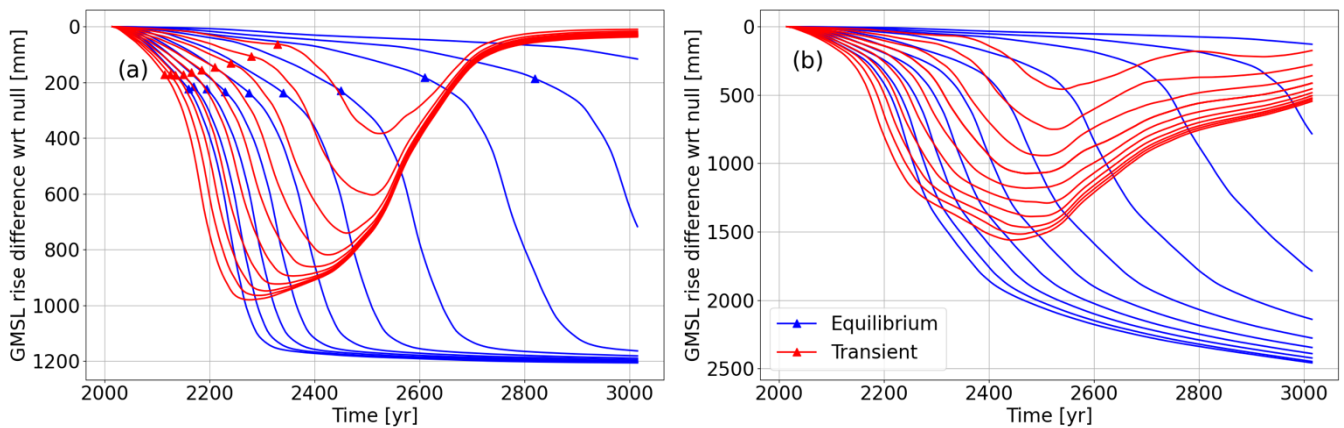
392 Figure 6 presents the integrated GMSL rise resulting from the schematic warming experiments, for both the ASE and the entire
393 AIS. Starting from the transient initialization, applying a uniform and abrupt ocean warming to the ASE triggers an earlier
394 onset of collapse with increasing temperatures, with diminishing sensitivity at higher ocean temperatures, but a larger rate of
395 GMSL rise. The impact of ocean warming is larger in simulations initialized without present-day mass change rates. This can
396 be attributed to the optimized parameter δT , which tends to be lower in these runs. As a result, adding 0.2 K of ocean warming
397 leads to a relatively larger increase in effective ocean temperatures compared to simulations that include present-day mass
398 change rates, where δT is typically higher.

399

400 Interestingly, the equilibrium simulations (blue lines in Fig. 6) show a greater long-term GMSL contribution from the AIS
401 compared to the transient simulations. The equilibrium runs are more sensitive to ocean warming, which can be partly
402 attributed to a larger relative increase in δT , and to the stabilizing effect of including present-day mass change rates.
403 Specifically, incorporating these rates makes the Kamb Ice Stream (see Fig S6) more stable, as it is currently thickening (Smith
404 et al., 2020). A more stable Kamb ice stream acts as a brake on the retreat of Siple Coast glaciers once the ASE has lost its
405 grounded ice. In this scenario, the retreat of the grounding line and subsequent ice sheet collapse are less able to propagate
406 beyond the ASE, across the WAIS ice divide, and into the Siple Coast region. In contrast, in the equilibrium simulations, where
407 this stabilizing effect is absent, such large-scale collapse can occur more easily.

408

409



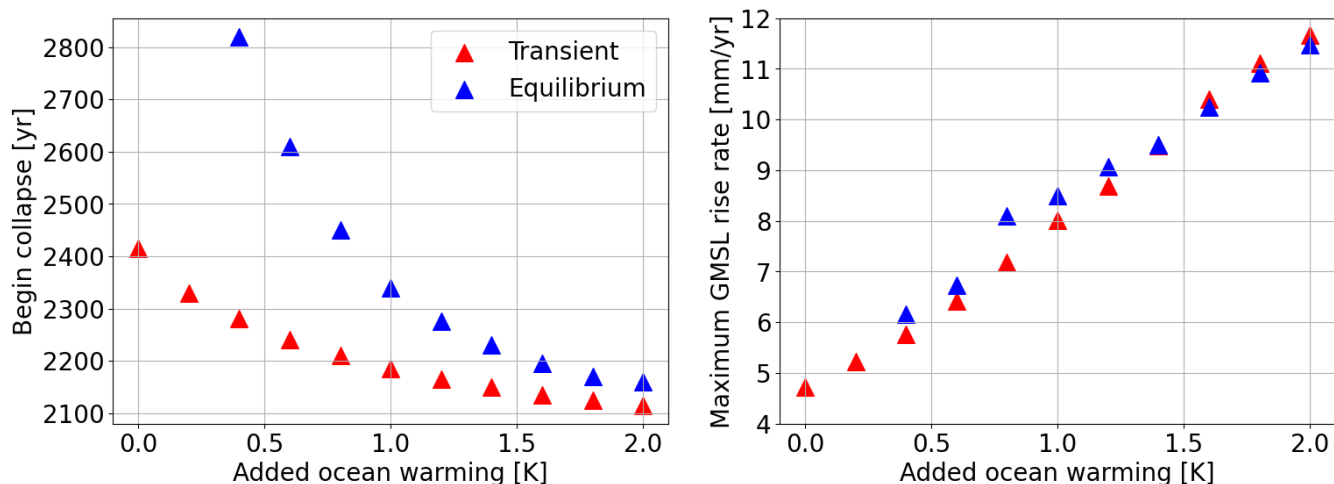
410

411 **Figure 7. All schematic warming scenarios with the control experiment (i.e. 0 ocean warming) subtracted.** For the ASE (a) and the
412 AIS (b) in terms of GMSL rise. Triangles indicate the timestep when the ridge in the bedrock approximately 45 km inland of the present-
413 day TG grounding line ungrounds, depicted by the line AB in Fig S6. Red lines indicate simulations starting with the observed mass change
414 rates, blue lines indicate simulations starting from an equilibrium. From right to left (later collapse to earlier collapse) the simulations are

415 forced with 0.2 to 2 K of ocean warming with steps of 0.2 K. Triangles indicate the timesteps when the line AB in Fig S6 ungrounds
416 completely.

417 To investigate the impact of different initial conditions, we subtracted the results of the no-perturbation simulations (i.e. 0 K
418 of added ocean warming in the ASE) from their corresponding schematically forced simulations (Figure 7). In the case of the
419 equilibrium initialization, the no-perturbation experiment resulted in negligible mass loss, so the mass loss in the forced
420 experiments due to the applied ocean forcing is almost the same as the difference between the forced scenarios and the no-
421 perturbation experiment. In contrast, the unforced transient initialization exhibits a collapse of the WAIS, so Figure 7 shows
422 the deviation from this evolution due to the added ocean forcing.

423 The simulations starting from the transient initialization have a much different response than those starting from the
424 equilibrium initialization. For the first 250 (strong forcing) to 600 (weak forcing) years, the impact of ocean warming is larger
425 for the transient initialisation simulations than for the equilibrium initialization simulations. Positive feedbacks drive the
426 collapse of the WAIS, and these feedbacks are initiated earlier if the simulations start out-of-balance. After the collapse of TG
427 and PIG, the impact of ocean warming ceases in the transient initializations simulations, as the GMSL rise contribution slows
428 down in the final phase of the collapse (Fig. 6b) and the WAIS can only collapse once. This ceasing effect will not occur for
429 the equilibrium initialization simulations, as the ocean forcing induces all the GSML rise contribution and the collapse of the
430 WAIS, which otherwise would not happen.



431
432 **Figure 8. Impact of ocean warming on the beginning of the collapse and maximum GMSL rate.** (left) The beginning of the WAIS
433 collapse defined as the ungrounding of ridge AB in Van Den Akker et al. (2025b) as function of added uniform and sudden ocean warming
434 in the ASE. Blue dots represent simulations. (right) the maximum GMSL rise rate modelled in the same simulations, also as function of the
435 added ocean warming.

437 In Figure 8, increasing ocean warming is correlated with an earlier onset of TG collapse, which in our simulations consistently
438 acts as the precursor to WAIS collapse. In this study, all collapse events initiate at TG. The onset of collapse is defined as the
439 first timestep at which the bedrock ridge, 50 km upstream the current grounding line (see Figure S6) becomes entirely free of
440 grounded ice. The role of this bedrock ridge is discussed in more detail by Van Den Akker et al. (2025b). The results show an
441 that higher ocean temperatures lead to earlier collapse, but with progressively smaller shifts in timing. This suggests the
442 presence of a limit on the onset of collapse, TG cannot collapse before ~2100 without more than 2 degrees of ocean warming.
443 Meanwhile, the maximum GMSL rise rate during the collapse increases linearly with ocean temperature, indicating that while
444 earlier collapse timing shows diminishing returns, the rate of sea-level rise keeps on intensifying with stronger forcing. The
445 additional sea-level contribution can come not only from PIG and TG, but also from the neighbouring Pope, Smith and Kohler
446 glaciers, which are in the same basin as TG and therefore receive the same ocean warming. Furthermore, simulations starting
447 from an ice sheet in equilibrium have the collapse delayed by multiple centuries compared to the transient initialization
448 simulations. Here, however, warmer ocean waters still bring the collapse onset forward, without approaching a limit. It is
449 noteworthy that the maximum GSML rise rate, if reached, is comparable to transient initialization runs.

450

451 **3.2 Realistically forced Future Antarctic Mass change**

452 Figure 9 shows the simulated integrated ice sheet mass loss in the Amundsen Sea Embayment (ASE) as well as for the entire
453 Antarctic Ice Sheet. Until 2150, the projected mass loss is largely determined by the initialisation method; hence the current
454 dynamic imbalance sets the 'short term' mass loss of the ASE. After 2150, all simulations project eventual WAIS collapse, in
455 most cases before 2500. Simulations initialized with the transient initialization configuration (solid lines) predict faster ice
456 mass loss and an earlier collapse than those initialized with the equilibrium initialization configuration (dashed lines). This
457 accelerated ice mass loss when using the transient initialization compared to the equilibrium initialization and collapse due to
458 transient initialization occurs 50 to 100 years earlier under low emission scenarios (SSP126 or RCP26) and 25 to 50 years
459 earlier under high-emission scenarios. These findings highlight the impact of the present-day imbalance on WAIS projections
460 and emphasize the need to include those in regional simulations. The influence of this imbalance is more pronounced under
461 cooler scenarios, where future ocean warming and surface melting is less dominant. In warmer scenarios (RCP8.5 and SSP5-
462 85), the strong ocean forcing and net negative SMB diminishes the relative impact of model initialization choices. Similar
463 results have been described for glacial isostatic adjustment applications by Van Calcar et al. (2024) who argue that the details
464 of the GIA matter relatively more for small forcing and relatively less for strong forcing.

465

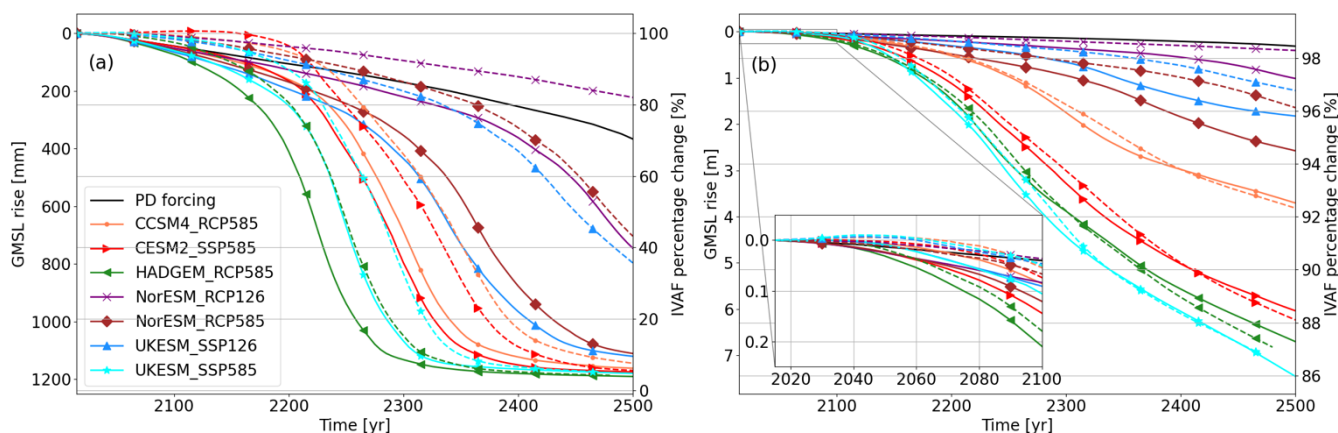
466 For the whole AIS and in the perspective of modelled multi-metre GMSL rise contribution, the present-day imbalance has an
467 impact on the AIS mass loss before 2100. All simulations starting from the transient initializations show more integrated mass
468 loss over the AIS in 2100 compared to the simulations starting from the equilibrium initialization, with in most cases a doubled
469 GMSL rise contribution when using the present-day observed mass change rates, except for the simulations forced by

470 HADGEM_RCP585 when considering the ASE region. This forcing contains early ocean warming and little increases in the
471 SMB in the beginning of the simulation, overshadowing almost immediately the differences caused by the transient and
472 equilibrium initialization with a much larger signal. However, simulations forced by both UKESM forcing datasets show the
473 largest and fastest increase in sea level rise over the whole AIS.

474
475 After 2150, the emission scenario has the largest impact on the projected mass loss, for the high-end and low-end scenarios
476 the projected GMSL rise is 1 – 6 and 1 – 2 m, respectively. The difference in projected ocean changes by various ESMs is the
477 next largest source of uncertainty, this will be discussed more below, Lastly, the effect of equilibrium or transient initialisations
478 on the projected GMSL rise from the AIS is, in relative sense, profoundly smaller than in regional simulations focussing on
479 the ASE, or on short term projections of the AIS. In 2500 for the whole AIS, the difference between transient and equilibrium
480 starting runs is about 1-2 % IVAF change. At a regional ASE simulation and before 2500, the difference can be up to 10-20%
481 IVAF, a tenfold difference.

482
483 For high-emission scenarios, incorporating the mass change rates even decreases the GMSL rise contribution. This can be
484 explained by the strength of the warming in these scenarios, which leads to the collapse of major ice shelves in both transient
485 and equilibrium initialized simulations. At the same time, observed thickening in parts of the grounded East Antarctic Ice
486 Sheet (EAIS) continues in the future simulations, offsetting some of the mass loss from West Antarctica. As a result, mass loss
487 in the WAIS is partially balanced by the increase in thickness in Dronning Maud Land, yielding a similar projected GMSL
488 rise contribution, see Figure 9. We argue that the spatial distribution of mass change in the transient initialization simulations
489 is more physically justified compared to the pattern of mass loss in the equilibrium initialization cases, since the former
490 captures a projected thickening of the EAIS until 2100, in line with recent studies on the forced future of the modelled Antarctic
491 Ice Sheet (Siahaan et al., 2022; Coulon et al., 2024; Klose et al., 2024; O'Neill et al., 2025) and in line with present-day
492 observations (Smith et al., 2020).

493
494 The simulations forced with NorESM output (RCP126 and RCP585) show much less mass loss than the others, as both
495 NorESM simulations have less warming and more enhanced accumulation than the other ESM runs. The NorESM output
496 assumes a constant climate after 2100, while output from the other ESMs assumes ongoing warming through 2300.



498

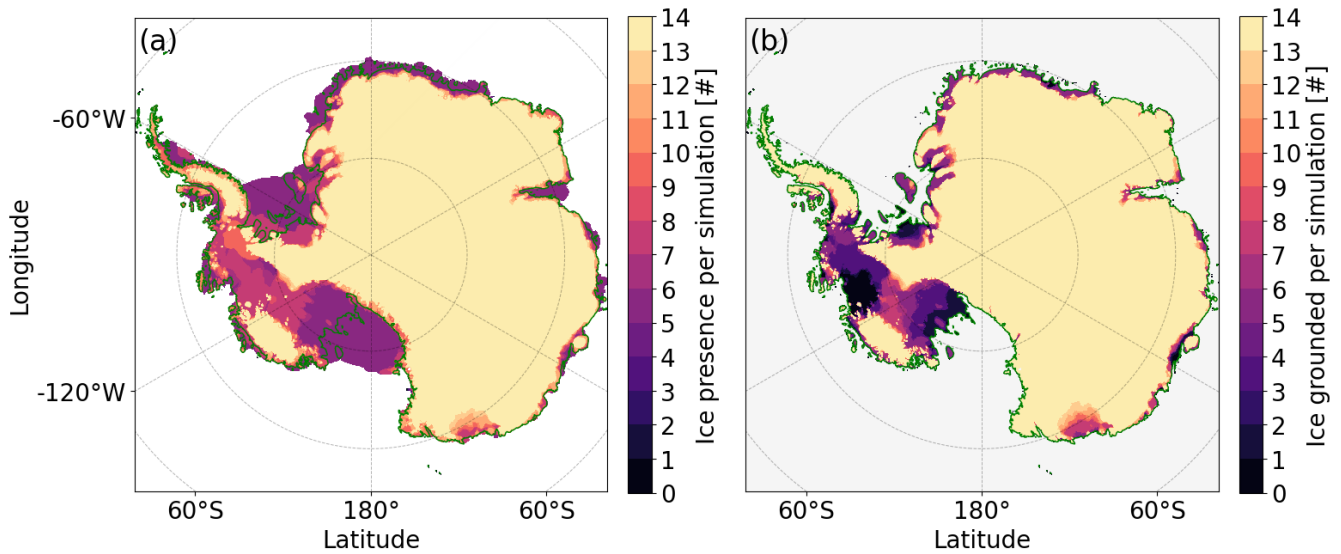
499 **Figure 9.** Integrated mass loss in the ASE, where Thwaites Glacier and Pine Island Glacier are situated (a). Left y-axis shows the GMSL
 500 rise in mm and right y-axis the Ice Volume Above Floatation in percentage of the initial value. The same for the whole AIS (b). Solid lines
 501 indicate simulations starting with the observed mass change rates, dashed lines indicate simulations starting from an equilibrium. Colors
 502 indicate the ocean forcing scenario used. The black line indicates an unforced transient initialization simulation. PD-forcing denotes a
 503 simulation without any additional ESM forcing, similar to what was done by Van Den Akker et al. (2025b)

504

505 Next, we discuss the modelled patterns of ice shelf and grounding line retreat. Figure 10 shows the number of simulations
 506 containing ice (Fig. 10a) and grounded ice (Fig. 10b) across Antarctica for the year 2500. The most significant reduction in
 507 grounded ice area occurs in WAIS. Aside from Wilkes Land, the grounding line retreat is limited in the EAIS as for most of
 508 the coastline, the inland bedrock is close to or above sea level. All simulations predict substantial grounded ice loss in Thwaites
 509 Glacier, as already clear from Figure 6a. While not all scenarios result in a full WAIS collapse, several high-emission scenarios
 510 show complete loss of floating ice at the current locations of PIG and TG.

511

512 For half the simulations, the Filchner Ronne shelf and the Bungenstock Ice Rise (near the Southern margin of the Ronne ice
 513 shelf) have respectively disappeared and completely ungrounded by 2500. Even more than half (9 out of 14) simulations end
 514 with the Ross shelf completely melted, in some cases along with glaciers at the Siple coast. As our simulations do not model
 515 calving for retreated ice shelves, this disintegration is entirely due to enhanced basal melting by warmer ocean waters. In fact,
 516 in simulations where the Filchner-Ronne or the Ross shelves disintegrate, the Bungenstock Ice Rise or the Siple Coast also
 517 deglaciate, showing a direct relation between the large floating ice shelves and their upstream tributary glaciers.



519

520 **Figure 10.** Ice present (a) and grounded (b) at the end (2500) of every simulation per grid cell, summed over all 14 simulations: with 7 ESM
 521 scenarios and the 'transient and equilibrium initialization.

522

523 This clear connection between floating and grounded ice mass is further assessed in Figure 11. The floating ice mass and
 524 percent change of IVAF since 2015 are shown per region (Filchner-Ronne, Ross and ASE as delineated in Fig. S3) in this
 525 figure. Both the Filchner-Ronne and Ross shelves display similar trends. Some ESM forcings result in little change in modelled
 526 floating ice mass on the shelves during the simulation. For the Ross shelf, this occurs under UKESM-SSP126 and
 527 NorESM_RCP26, while for Filchner-Ronne the same applies with the addition of NorESM_RCP85. In all other scenarios
 528 except NorESM_RCP85 for Ross, the volume of floating ice diminishes. This pattern is irrespective of the transient or
 529 equilibrium initialization: the dashed and solid lines in Figure 11 show little difference. These regions are currently relatively
 530 stable compared to the ASE (Smith et al., 2020). As a result, incorporating the small observed mass change rates in those
 531 regions does not affect the mass loss in future projections.

532

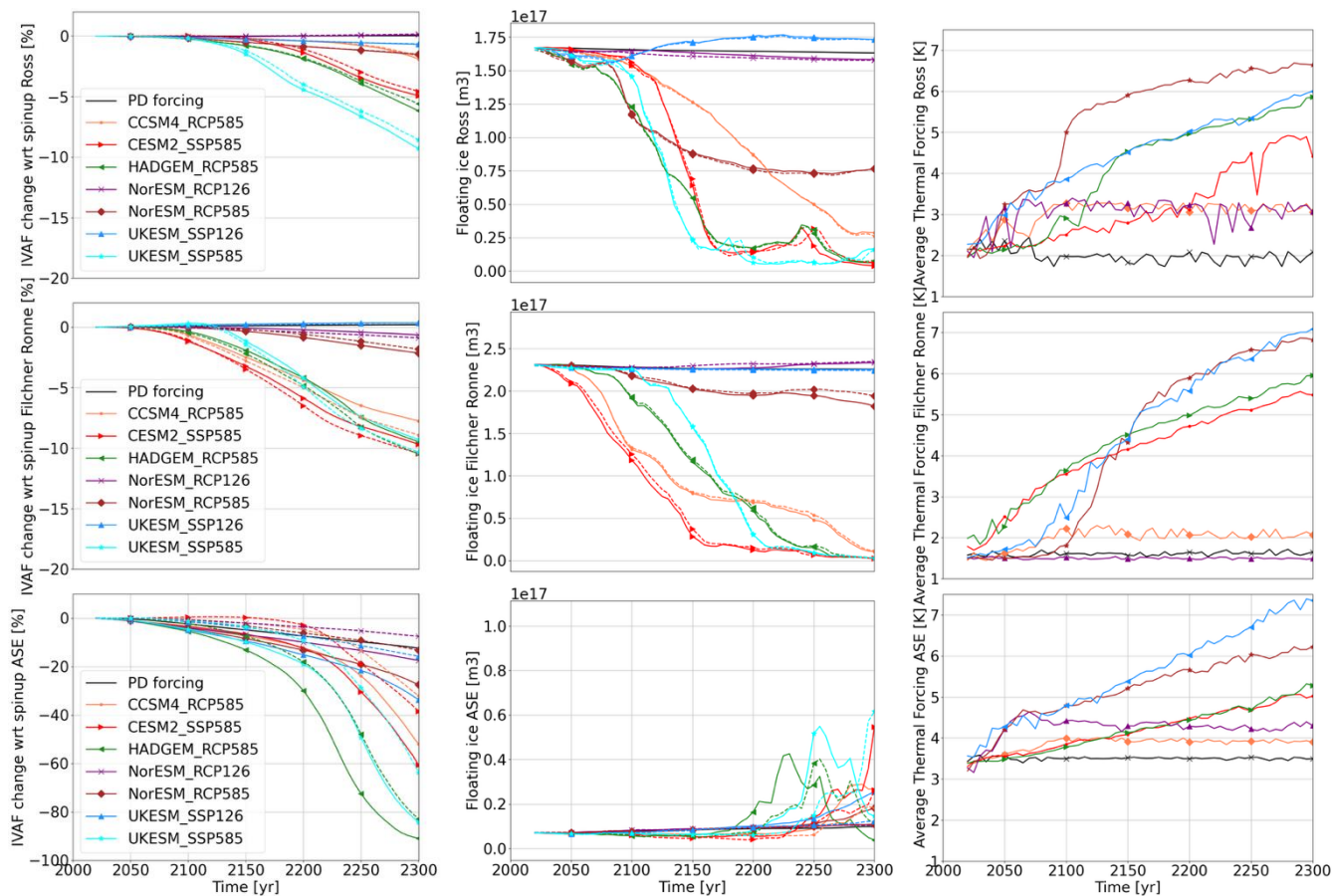
533 The loss of floating ice mass is closely tied to the average thermal forcing in each region, as shown in Figure 11. For the
 534 Filchner-Ronne shelf, the percent change in IVAF, the floating ice mass loss and the average thermal forcing all follow a
 535 consistent pattern. Some ESMs simulate increased thermal forcing at the FR calving front, which leads to near-complete shelf
 536 collapse and substantial ice mass loss. Others maintain thermal forcing near present-day levels, resulting in a largely intact ice
 537 shelf and minimal mass loss. A similar pattern is observed for the Ross shelf, the middle column in Figure 11. The notable
 538 exception is NorESM_RCP85, which leads to a reduced Ross shelf in 2300 but not to a complete loss. In this simulation,
 539 thermal forcing rises sharply between 2050 and 2100 before stabilizing, which results from repeated climate forcing applied

540 to the NorESM simulations. The early spike is enough to halve the shelf volume quickly, the subsequent stabilization allows
 541 the remaining half to persist.

542

543 The ASE region exhibits a distinct pattern. At the beginning of each simulation, there is little floating ice present in the PIG
 544 and TG basins. The present-day shelves are small compared to FR and Ross. As soon as the grounding line starts to retreat and
 545 the grounding line flux increases, a large shelf is formed. However, if the thermal forcing is strong enough, this newly formed
 546 shelf rapidly melts, producing the increasing and then decreasing pattern of floating ice mass loss in the bottom row of Figure
 547 11. Van Den Akker et al. (2025a) provide a more detailed discussion of the role of the shelves on the future dynamics of TG.

548



549

550 **Figure 11. Ice volume above floatation (IVAF), floating ice mass and average thermal forcing for Ross (upper row),**
 551 **Filchner Ronne (middle row) and ASE (bottom row) per basin until 2300.** The left column shows the IVAF as a percentage
 552 of what was present at the initialization; the middle column shows the total mass of floating ice per region; the right column
 553 shows the average thermal forcing at 510 m below sea level at the calving front.

554

555 The loss of grounded ice mass and the reduction in floating ice volume are similarly related for the Ross and Filchner-Ronne
556 basins. Once a critical fraction of floating ice is lost, the buttressing declines, leading to accelerated upstream flow of grounded
557 ice, contributing to GMSL rise. To estimate this time lag between the onset of floating ice mass reduction and grounded ice
558 loss, we calculated the time delay between 10% floating ice mass loss of an ice shelf sector and 5 % grounded ice mass loss
559 from that sector for each simulation and for the Filchner-Ronne and Ross sectors. We excluded the ASE from this analysis as
560 in this region buttressing has currently little impact on the ice dynamics (Favier et al., 2014; Robel et al., 2019; Lipscomb et
561 al., 2021; Gudmundsson et al., 2023; Van Den Akker et al., 2025b). Typically, the delay between losing 10% of floating ice
562 and 5% grounded ice loss is in the order of decades (Table 4). In general, glaciers feeding into the Filchner-Ronne Ice Shelf
563 respond slightly more rapidly than those along the Siple Coast, indicating that the Filchner-Ronne shelf provides a little more
564 buttressing. Therefore, once 10% of the Filchner-Ronne’s floating ice volume is lost compared to present-day levels, most
565 simulations show that 5% of grounded ice mass loss (58.7 cm GMSL rise) will follow.

566
567 Except for NorESM_RCP85, the delay in deglaciation of the FRIS is higher when doing a transient initialization compared to
568 simulations starting from the equilibrium simulation, while the delay for Ross is often shorter. This is due to an opposite pattern
569 in the mass change rates of Smith et al. (2020). The Filchner-Ronne shelf is currently thinning, but the grounded ice upstream
570 is slowly thickening. This is reversed at the Siple Coast and the Ross ice shelf: here the shelf is thickening and the grounded
571 ice mainly thinning. Adding the mass change rates as was done for the transient initialization makes the grounded ice upstream
572 of the Filchner-Ronne shelf slightly more stable and at the Siple Coast slightly less stable, and therefore slightly more sensitive
573 to floating ice mass loss.

574
575 Significant floating ice volume loss leads in most cases within a century to significant grounded ice loss and sea level rise.
576 This can be explained by two mechanisms: the sensitivity of the basal melt parameterization to changes in the ocean
577 temperatures (e.g. the sum of TF_{base} and δT in Eq. (1.5)) and the location of large SMB anomalies. Regarding the former,
578 when deriving Eq. (1.6) with respect to the sum of TF_{base} and δT and filling in parameter values, we find that the basal melt
579 parameterization has a temperature change sensitivity of $\sim 11 \text{ m yr}^{-1} \text{ K}^{-1}$ when the sum of TF_{base} and δT is 1 K, increasing
580 linearly (e.g., when the sum is 2 K, the melt sensitivity is $22 \text{ m yr}^{-1} \text{ K}^{-1}$). For some scenarios, the ocean forcing applied can be
581 several degrees K, causing an increase in basal melt of hundreds of metres per year, while the SMB anomalies range only from
582 -2 to 2 m yr^{-1} .

583
584
585
586

587 **Table 4. Delay in years between a floating ice mass loss of 10% and an IVAF loss of 5% (5% translates to 58.7 cm**
588 **GMSL rise from FRIS and 24.4 cm from Ross).** The symbol ‘x’ denotes simulations when the 10% ice volume above
589 floatation threshold and/or the 100 mm SLR contribution is never reached. The Filchner-Ronne shelf is abbreviated with
590 ‘FRIS’, the Ross shelf with ‘Ross’.

ESM forcing	Transient initialization delay (yr)		Equilibrium initialization delay (yr)	
	FRIS	Ross	FRIS	Ross
CCSM4_RCP85	145	280	130	305
CESM2_SSP585	130	195	120	210
HADGEM_RCP85	120	200	110	210
NorESM_RCP26	x	x	x	x
NorESM_RCP85	320	x	x	x
UKESM_SSP126	x	x	x	x
UKESM_SSP585	100	120	80	120

591

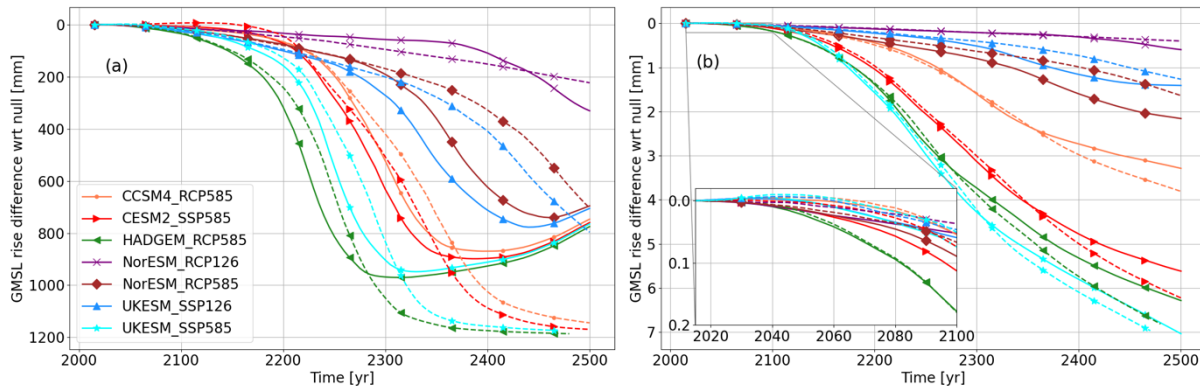
592

593 Finally, in Figure 12, we investigate if the present-day imbalance adds up linearly to future climate forcing, by subtracting the
594 no-forcing experiment from all forced experiments. Compared to Figure 7, the differences between the transient and
595 equilibrium simulations are much less pronounced, hence the long term impact of the current imbalance and future warming
596 looks to add up largely linearly. Only when the transiently initialized simulation is in the collapse phase of TG and PIG, the
597 ESM forcing causes a non-linear enhancement of the GMSL rise contribution from the ASE sector (Fig. 12a). This is caused
598 by enhanced ocean warming in the ASE sector compared to the initializations, which is most pronounced in the
599 HADGEM_RCP85 scenarios. The other simulations shown in Fig 12 that show a distinct difference in response between the
600 equilibrium and transient simulations are UKESM_SSP585 and CESM2_SSP585, both of which include severe drops in the
601 surface mass balance over the grounding line are of the ASE sector (see Fig 2.). All other ESM forcing datasets contain a
602 smaller difference in ocean temperature with the spinup (see Fig 1.), as well as smaller SMB anomalies, and therefore show a
603 less pronounced difference with their respective control scenario.

604

605 Prior to the collapse phase, the simulations align much more closely than in Figure 7. This may be explained by the fact that,
606 as the TG and PIG basins approach collapse, their mass loss becomes increasingly governed by ice dynamics and less by
607 external forcings. Consequently, simulations starting from equilibrium conditions are more sensitive to gradual warming,
608 which corresponds to the faster increase in GMSL contribution observed in the transiently initialized simulations (Fig. 11,
609 bottom row). As in Figure 7a, the influence of the ESM forcing ceases after the collapse, since WAIS also collapses in the
610 transient simulation without forcing, demonstrating that WAIS can only collapse once. Lastly, the difference between the

611 transiently and equilibrium-initialized simulations is minimal for the AIS as a whole (Fig. 12b), as the substantial projected
 612 GMSL contribution by 2500 from AIS primarily originates from regions outside the ASE sector, which currently remain in
 613 balance (Fig. 11).
 614



615
 616 **Figure 12. Induced mass loss by the ESM forcings with respect to the unforced simulations**, for (a) the ASE and (b) the AIS in terms
 617 of GMSL rise. Solid lines indicate simulations starting with transient initialisation, dashed lines indicate simulations starting from the
 618 equilibrium initialisation. Colors indicate the ocean forcing scenario used.

619
 620

621 4. Discussion

622 In this study, we show that including the observed present day mass change rates in an ice sheet model (CISM) improves the
 623 quality of projected ice mass loss for the coming century (up until 2100), because it is consistent with the currently observed
 624 GMSL rise contribution. Before 2100, including the present-day mass change rates lead to considerably higher GMSL rise
 625 contributions from the AIS, regardless of the ESM forcing chosen. After 2100, dynamic effects like a TG and PIG collapse
 626 start to develop, leading to accelerating mass loss. Including the present-day mass change rates accelerates a modelled WAIS
 627 collapse by 25 to 100 years in forced simulations. In 2500 for the whole AIS, the difference between transient and equilibrium
 628 starting runs is about 1-2 % IVAF change. In regional ASE simulations and before 2500, the difference can be up to 10-20%
 629 IVAF, a tenfold difference.

630

631 At the start of our simulations, we find a sea level rise rate in the order 0.1 – 0.5 mm per year, when using the transient
 632 initialization method. This is in line with the observed rates reported by Cronin (2012); Smith et al. (2020); Fox-Kemper et al.
 633 (2021). In 2100, our spread in projected sea level rise from the WAIS and AIS is about 5 – 25 mm is comparable to the present-
 634 day observed rate (approximately 0.3 mm yr⁻¹) and in line with Van De Wal et al. (2022). This range is similar to values
 635 reported by Edwards et al. (2021); Coulon et al. (2024); Klose et al. (2024); Seroussi et al. (2023); O'Neill et al. (2025). In our
 636 ensemble, we do not find any cases where the AIS gains net mass during our simulated period, contrasting results found by

637 Siahaan et al. (2022). They found increased snowfall to dominate over increased basal melting, which leads to a net mass gain
638 until 2100, with higher mass gains with warmer climates. However, in simulations done with low climate forcing, they found
639 a steady decrease of ice mass at the WAIS, similar to the results presented in this study. When continued, this could in their
640 simulation lead to the Marine Ice Sheet Instability and further enhanced mass loss beyond 2100, possibly outpacing mass gain
641 through increased snowfall.

642
643 In 2300, our modelled ensemble shows a GMSL rise contribution of roughly 100 – 1200 mm from the WAIS and 100 – 4500
644 mm for the entire Antarctic ice sheet. This large range is caused by dynamic instabilities caused by ice sheet thinning earlier
645 in the simulation. Our ensemble almost captures the range reported by Seroussi et al. (2024); Greve et al. (2023); Payne et al.
646 (2021), with the exception of the cases where the AIS is growing (i.e., when a negative GMSL rise contribution is simulated).
647 The dynamic instability leading to the WAIS collapse is featured in all our simulations, causing large mass losses and thereby
648 compensating any (small) mass gains on the EAIS. Furthermore, the ESM forcing used shows predominantly warming ocean
649 waters and a decreasing SMB over the whole AIS from present-day until 2300 with time, in contrast to Siahaan et al. (2022),
650 in whose simulations till 2100 the SMB increase dominates over ice dynamical processes.

651
652 Our schematic experiments show that simulations initialized with present-day mass change rates respond less strongly to
653 schematic and uniform ocean warming than those using equilibrium initializations. As expected, greater ocean warming
654 triggers an earlier collapse of TG and, subsequently, the ASE basin but with diminishing returns: the most significant impact
655 of additional warming is seen in the low-warming scenarios. Notably, the onset of collapse does not occur before 2100, even
656 with 2 degrees of ocean warming. This is in agreement with earlier WAIS collapse studies, Joughin et al. (2014) mention from
657 2200 onward, Robel et al. (2019) and Van Den Akker et al. (2025b) mention approximately 500 years onward. This suggests
658 a potential ice dynamical threshold that delays the TG collapse. However, the peak rate of GMSL rise during the collapse
659 continues to increase linearly with additional ocean warming. This aligns with the contrasting patterns in Figures 7 and 12:
660 while the non-linear enhancement of mass loss by additional ocean warming and present-day mass losses prior the collapse of
661 the ASE sector is very apparent in the idealized simulations, it is largely absent in the simulations forced with ESM data.
662 Hence, we find that including the present-day mass loss rates increases the modelled GMSL from the AIS mainly in the short
663 term when mass loss is dominated by the ASE.

664
665 The relative unimportance of the SMB changes is related to the location of their anomalies. The largest anomalies are found
666 near the coast of the AIS, where in many locations floating ice, or as the simulations progress, no ice at all exists. Therefore,
667 the increased/decreased SMB is not contributing significantly to changes in projected GMSL rise from simulations forced by
668 output from different ESMs. However, the SMB in the CMIP5 and CMIP6 models are determined using the present-day
669 geometry of the Antarctic Ice Sheet. In our simulations, the ice sheet geometry changes drastically, with surface heights
670 decreasing for most of the WAIS. Lower surfaces will through the lapse rate yield higher air temperatures and a more negative

671 SMB, which could enhance mass loss more when this effect is incorporated. Ideally, ice sheet modellers should use coupled
672 simulations where atmospheric models directly resolve the SMB of ice sheets based on their evolving geometries. This is
673 computationally expensive and only done for the AIS in recent UKESM studies, such as shown by Siahhan et al. (2022).
674 Alternatively simple parameterizations of this effect could be used (e.g. Fortuin and Oerlemans (1990)). A solution could be
675 to use SMB emulators, but these have yet to be developed.

676
677 In many simulations shown in our study, all floating ice disappears from the Filchner-Ronne and Ross shelves. This is not
678 uncommon in forced AIS simulations (Coulon et al., 2024; Seroussi, 2021; Seroussi et al., 2024). However, the disappearance
679 of the big ice shelves is controlled by the amount of warming available in their cavities. CISM does not contain a submodule
680 to simulate the overturning circulation in the ice shelf cavities, and neither did the ESMs from which the forcing was used in
681 this study. The thermal forcing was only available in the open ocean bounded by the (observed) calving front of the AIS, and
682 had to be extrapolated into the cavities. Therefore, it cannot be ruled out that the warming simulated in the cavities that lead
683 to dramatic floating ice loss of the large ice shelves is caused (at least in part) by the extrapolation scheme. In essence the
684 extrapolation scheme now determines when the ice shelf cavities shift from a cold cavity, which they are at present, to a warm
685 cavity. Future studies could improve this aspect by using cavity-resolving ocean models (Scott et al., 2023), or an intermediate
686 complexity 2D layer resolving model like LADDIE (Lambert et al., 2022).

687
688
689 In this study, we employed seven forcing datasets derived from five ESMs . Although forcing data were available only up to
690 the year 2300, our simulations extended to 2500. To enable CISM to run through 2500, we held the final available forcing
691 fields (from 2300) constant over the years 2300–2500. This approach could introduce biases if conditions in 2300 differ
692 substantially from those in the surrounding decades. To assess this, we compared the 20-year mean (2280–2300) thermal
693 forcing and surface mass balance (SMB) anomalies, shown in Figs S9 and S10, with the values used for the year 2300 (Figs 1
694 and 2). For ocean thermal forcing, the year-2300 fields closely match the 20-year mean across all datasets. SMB anomalies
695 show minor differences between the year 2300 and the average of 2280-2300, most notably in the NorESM_RCP26 dataset
696 over the Weddell Sea, but overall the spatial patterns and magnitudes remain highly similar. These comparisons suggest that
697 substituting the 20-year mean for the single year 2300 would not affect our results considerably.

698
699
700 We applied a no-advance calving approach: the calving front was restricted from advancing beyond its present-day observed
701 position. While it was allowed to retreat, primarily due to significant increases in basal melt rates observed in most simulations,
702 calving ceased entirely once the front retreated upstream of its current position. Although this is a conservative and somewhat
703 unphysical representation, it serves as a simplified framework. Incorporating a more physically grounded calving law,

704 accounting for factors such as stress and strain rates, rather than relying solely on modeled ice thickness, could improve
705 predictions of ice mass loss. Integrating such advanced calving schemes into CISM is an area of active research.

706

707 **5. Conclusion**

708 In this paper, we show ocean-forced Antarctic wide simulations conducted with the Community Ice Sheet Model until 2500.
709 We test a new feature of the model: initializing with the present-day observed mass change rates. Schematic ocean warming
710 causes a faster onset of TG collapse with diminishing returns but linearly increasing GMSL rise rates with additional warming.
711 We furthermore find that including the present-day imbalance is important for regional WAIS simulations, where including
712 the present-day mass change rates in a simulation speeds up Thwaites Glacier and Pine Island Glacier collapse by 25 – 100
713 years. Including the mass change rates doubles the AIS GMSL contribution in 2100 in our ensemble. For long-term continental
714 AIS simulations beyond 2100, the choice of the ESM used is more important than the choice to include or not the present-day
715 mass change rates in a century timescale simulation. We find for all simulations that the AIS will continue to lose mass over
716 the next five centuries, with uncertainties increasing strongly over time.

717

718 Our study highlights that, for simulations until 2500, the main ice losses happen in the Ross and Filchner-Ronne, preceded by
719 mass loss in the ASE region, but the pattern is highly dependent on the extrapolation scheme of ocean properties into the ice
720 shelf cavities. The mass balance of the floating ice shelves proves to be crucial for the grounded ice loss rate. In our simulations
721 we do not employ a physically based calving scheme or a sub-shelf cavity resolving ocean model. Replacing both processes
722 with physically based parameterizations or sub-models will likely change the mass balance of the floating shelves and
723 ultimately increase our confidence in sea level rise projections from the Antarctic Ice Sheet. Including a more physically based
724 rather than a location based calving flux will probably increase the modelled future mass loss of the AIS, and therefore project
725 faster ice sheet retreat and as a consequence, more GMSL rise.

726

727 **Code availability**

728 CISM is an open-source code developed on the Earth System Community Model Portal (EPSCOMB) Git repository available
729 at <https://github.com/ESCOMP/CISM>. The specific version used to run these experiments will be tagged before publication.

730

731 **Data availability**

732 The output of the simulations shown in this study will be uploaded to a Zenodo repository before publication.

733

734 **Author contributions**

735 TvdA designed and executed the main experiments. WHL and GRL developed CISM and helped configure the model for the
736 experiments. RSWvdW, WJvdB, WHL, GRL provided guidance and feedback. TvdA prepared the manuscript, with
737 contributions from all authors.

738
739
740
741
742
743
744
745
746

TvdA received funding from the NPP programme of NWO. WHL and GRL were supported by the NSF National Center for Atmospheric Research, which is a major facility sponsored by the National Science Foundation (NSF) under Cooperative Agreement no. 1852977. Computing and data storage resources for CISM simulations, including the Derecho supercomputer (<https://doi.org/10.5065/D6RX99HX>), were provided by the Computational and Information Systems Laboratory (CISL) at NSF NCAR. GRL received additional support from NSF grant no. 2045075.

The authors declare no competing interests.

747 References

748 Adusumilli, S., Fricker, H. A., Medley, B., Padman, L., and Siegfried, M. R.: Interannual variations in meltwater input to the
749 Southern Ocean from Antarctic ice shelves, *Nature geoscience*, 13, 616-620, 2020.

750 Amaral, T., Bartholomaus, T. C., and Enderlin, E. M.: Evaluation of iceberg calving models against observations from
751 Greenland outlet glaciers, *Journal of Geophysical Research: Earth Surface*, 125, e2019JF005444, 2020.

752 Aschwanden, A., Aðalgeirsdóttir, G., and Khroulev, C.: Hindcasting to measure ice sheet model sensitivity to initial states,
753 *The Cryosphere*, 7, 1083-1093, 2013.

754 Aschwanden, A., Bartholomaus, T. C., Brinkerhoff, D. J., and Truffer, M.: Brief communication: A roadmap towards credible
755 projections of ice sheet contribution to sea level, *The Cryosphere*, 15, 5705-5715, 2021.

756 Barthel, A., Agosta, C., Little, C. M., Hattermann, T., Jourdain, N. C., Goelzer, H., Nowicki, S., Seroussi, H., Straneo, F., and
757 Bracegirdle, T. J.: CMIP5 model selection for ISMIP6 ice sheet model forcing: Greenland and Antarctica, *The Cryosphere*,
758 14, 855-879, 2020.

759 Beckmann, A. and Goosse, H.: A parameterization of ice shelf–ocean interaction for climate models, *Ocean modelling*, 5, 157-
760 170, 2003.

761 Berdahl, M., Leguy, G., Lipscomb, W. H., Urban, N. M., and Hoffman, M. J.: Exploring ice sheet model sensitivity to ocean
762 thermal forcing and basal sliding using the Community Ice Sheet Model (CISM), *The Cryosphere*, 17, 1513-1543, 2023.

763

764 Berends, C. J., Goelzer, H., and Van De Wal, R. S.: The Utrecht finite volume ice-sheet model: UFEMISM (version 1.0),
765 *Geoscientific Model Development*, 14, 2443-2470, 2021.

766 Berends, C. J., Goelzer, H., Reerink, T. J., Stap, L. B., and Van De Wal, R. S.: Benchmarking the vertically integrated ice-
767 sheet model IMAU-ICE (version 2.0), *Geoscientific Model Development*, 15, 5667-5688, 2022.

768 Bett, D. T., Bradley, A. T., Williams, C. R., Holland, P. R., Arthern, R. J., and Goldberg, D. N.: Coupled ice/ocean interactions
769 during the future retreat of West Antarctic ice streams, *The Cryosphere Discussions*, 2023, 1-28, 2023.

770 Bradley, A. and Arthern, R.: WAVI. jl: A Fast, Flexible, and Friendly Modular Ice Sheet Model, Written in Julia, AGU Fall
771 Meeting Abstracts, C11A-03,

772 Choi, Y., Morlighem, M., Wood, M., and Bondzio, J. H.: Comparison of four calving laws to model Greenland outlet glaciers,
773 *The Cryosphere*, 12, 3735-3746, 2018.

774 Coulon, V., Klose, A. K., Kittel, C., Edwards, T., Turner, F., Winkelmann, R., and Pattyn, F.: Disentangling the drivers of
775 future Antarctic ice loss with a historically calibrated ice-sheet model, *The Cryosphere*, 18, 653-681, 2024.

776 Cronin, T. M.: Rapid sea-level rise, *Quaternary Science Reviews*, 56, 11-30, 2012.

777 Danabasoglu, G., Lamarque, J. F., Bacmeister, J., Bailey, D., DuVivier, A., Edwards, J., Emmons, L., Fasullo, J., Garcia, R.,
778 and Gettelman, A.: The community earth system model version 2 (CESM2), *Journal of Advances in Modeling Earth Systems*,
779 12, e2019MS001916, 2020.

780 DeConto, R. M., Pollard, D., Alley, R. B., Velicogna, I., Gasson, E., Gomez, N., Sadai, S., Condron, A., Gilford, D. M., and
781 Ashe, E. L.: The Paris Climate Agreement and future sea-level rise from Antarctica, *Nature*, 593, 83-89, 2021.

782 Edwards, T. L., Nowicki, S., Marzeion, B., Hock, R., Goelzer, H., Seroussi, H., Jourdain, N. C., Slater, D. A., Turner, F. E.,
783 and Smith, C. J.: Projected land ice contributions to twenty-first-century sea level rise, *Nature*, 593, 74-82, 2021.

784 Favier, L., Jourdain, N. C., Jenkins, A., Merino, N., Durand, G., Gagliardini, O., Gillet-Chaulet, F., and Mathiot, P.:
785 Assessment of sub-shelf melting parameterisations using the ocean–ice-sheet coupled model NEMO (v3. 6)–Elmer/Ice (v8.
786 3), *Geoscientific Model Development*, 12, 2255-2283, 2019.

787 Favier, L., Durand, G., Cornford, S. L., Gudmundsson, G. H., Gagliardini, O., Gillet-Chaulet, F., Zwinger, T., Payne, A., and
788 Le Brocq, A. M.: Retreat of Pine Island Glacier controlled by marine ice-sheet instability, *Nature Climate Change*, 4, 117-121,
789 2014.

790 Fortuin, J. and Oerlemans, J.: Parameterization of the annual surface temperature and mass balance of Antarctica, *Annals of*
791 *Glaciology*, 14, 78-84, 1990.

792 Fox-Kemper, B., H.T. Hewitt, C. X., Aðalgeirsdóttir, G., Drijfhout, S. S., Edwards, T. L., Golledge, N. R., Hemer, M., Kopp,
793 R. E., Krinner, G., Mix, A., Notz, D., Nowicki, S., Nurhati, I. S., Ruiz, L., Sallée, J.-B., Slangen, A. B. A., and Yu, Y.: Ocean,
794 Cryosphere and Sea Level Change. In *Climate Change 2021: The Physical Science Basis. Contribution of Working Group I*
795 *to the Sixth Assessment Report of the Intergovernmental Panel on Climate Change* Cambridge University Press, Cambridge,
796 United Kingdom and New York, NY, USA, 1211-1362, 2021.

797 Goldberg, D. N.: A variationally derived, depth-integrated approximation to a higher-order glaciological flow model, *Journal*
798 *of Glaciology*, 57, 157-170, 2011.

799 Greene, C. A., Gardner, A. S., Schlegel, N.-J., and Fraser, A. D.: Antarctic calving loss rivals ice-shelf thinning, *Nature*, 609,
800 948-953, 2022.

801 Greve, R. and Blatter, H.: Comparison of thermodynamics solvers in the polythermal ice sheet model SICOPOLIS, *Polar*
802 *Science*, 10, 11-23, 2016.

803 Greve, R., Chambers, C., Obase, T., Saito, F., Chan, W.-L., and Abe-Ouchi, A.: Future projections for the Antarctic ice sheet
804 until the year 2300 with a climate-index method, *Journal of Glaciology*, 69, 1569-1579, 10.1017/jog.2023.41, 2023.

805 Gudmundsson, G., Krug, J., Durand, G., Favier, L., and Gagliardini, O.: The stability of grounding lines on retrograde slopes,
806 *The Cryosphere*, 6, 1497-1505, 2012.

807 Gudmundsson, G. H., Barnes, J. M., Goldberg, D., and Morlighem, M.: Limited impact of Thwaites Ice Shelf on future ice
808 loss from Antarctica, *Geophysical Research Letters*, 50, e2023GL102880, 2023.

809 Joughin, I., Smith, B. E., and Medley, B.: Marine ice sheet collapse potentially under way for the Thwaites Glacier Basin,
810 *West Antarctica*, *Science*, 344, 735-738, 2014.

811 Joughin, I., Smith, B. E., and Schoof, C. G.: Regularized Coulomb friction laws for ice sheet sliding: Application to Pine Island
812 Glacier, Antarctica, *Geophysical research letters*, 46, 4764-4771, 2019.

813 Jourdain, N. C., Asay-Davis, X., Hattermann, T., Straneo, F., Seroussi, H., Little, C. M., and Nowicki, S.: A protocol for
814 calculating basal melt rates in the ISMIP6 Antarctic ice sheet projections, *The Cryosphere*, 14, 3111-3134, 2020.

815 Klose, A. K., Coulon, V., Pattyn, F., and Winkelmann, R.: The long-term sea-level commitment from Antarctica, *The*
816 *Cryosphere*, 18, 4463-4492, 2024.

817 Lambert, E., Jüling, A., Van De Wal, R. S., and Holland, P. R.: Modeling Antarctic ice shelf basal melt patterns using the one-
818 Layer Antarctic model for Dynamical Downscaling of Ice–ocean Exchanges (LADDIE), *The Cryosphere Discussions*, 2022,
819 1-39, 2022.

820 Leguy, G., Asay-Davis, X., and Lipscomb, W.: Parameterization of basal friction near grounding lines in a one-dimensional
821 ice sheet model, *The Cryosphere*, 8, 1239-1259, 2014.

822 Leguy, G. R., Lipscomb, W. H., and Asay-Davis, X. S.: Marine ice sheet experiments with the Community Ice Sheet Model,
823 *The Cryosphere*, 15, 3229-3253, 2021.

824 Levermann, A., Albrecht, T., Winkelmann, R., Martin, M., Haseloff, M., and Joughin, I.: Kinematic first-order calving law
825 implies potential for abrupt ice-shelf retreat, *The Cryosphere*, 6, 273-286, 2012.

826 Li, L., Aitken, A. R. A., Lindsay, M. D., and Kulesa, B.: Sedimentary basins reduce stability of Antarctic ice streams through
827 groundwater feedbacks, *Nature Geoscience*, 15, 645-650, 10.1038/s41561-022-00992-5, 2022.

828 Lipscomb, W. H., Leguy, G. R., Jourdain, N. C., Asay-Davis, X., Seroussi, H., and Nowicki, S.: ISMIP6-based projections of
829 ocean-forced Antarctic Ice Sheet evolution using the Community Ice Sheet Model, *The Cryosphere*, 15, 633-661, 2021.
830

831 Lipscomb, W. H., Price, S. F., Hoffman, M. J., Leguy, G. R., Bennett, A. R., Bradley, S. L., Evans, K. J., Fyke, J. G., Kennedy,
832 J. H., and Perego, M.: Description and evaluation of the community ice sheet model (CISM) v2. 1, *Geoscientific Model
833 Development*, 12, 387-424, 2019.

834 Meehl, G. A., Senior, C. A., Eyring, V., Flato, G., Lamarque, J.-F., Stouffer, R. J., Taylor, K. E., and Schlund, M.: Context for
835 interpreting equilibrium climate sensitivity and transient climate response from the CMIP6 Earth system models, *Science
836 Advances*, 6, eaba1981, 2020.

837 Morlighem, M., Rignot, E., Seroussi, H., Larour, E., Ben Dhia, H., and Aubry, D.: A mass conservation approach for mapping
838 glacier ice thickness, *Geophysical Research Letters*, 38, 2011.

839 Morlighem, M., Rignot, E., Binder, T., Blankenship, D., Drews, R., Eagles, G., Eisen, O., Ferraccioli, F., Forsberg, R., and
840 Fretwell, P.: Deep glacial troughs and stabilizing ridges unveiled beneath the margins of the Antarctic ice sheet, *Nature
841 Geoscience*, 13, 132-137, 2020.

842 Mottram, R., Hansen, N., Kittel, C., Van Wessem, J. M., Agosta, C., Amory, C., Boberg, F., Van De Berg, W. J., Fettweis, X.,
843 and Gossart, A.: What is the surface mass balance of Antarctica? An intercomparison of regional climate model estimates, *The
844 Cryosphere*, 15, 3751-3784, 2021.

845 Nowicki, S., Payne, A. J., Goelzer, H., Seroussi, H., Lipscomb, W. H., Abe-Ouchi, A., Agosta, C., Alexander, P., Asay-Davis,
846 X. S., and Barthel, A.: Experimental protocol for sealevel projections from ISMIP6 standalone ice sheet models, *The
847 Cryosphere Discussions*, 2020, 1-40, 2020.

848 Nowicki, S. M., Payne, A., Larour, E., Seroussi, H., Goelzer, H., Lipscomb, W., Gregory, J., Abe-Ouchi, A., and Shepherd,
849 A.: Ice sheet model intercomparison project (ISMIP6) contribution to CMIP6, *Geoscientific model development*, 9, 4521-
850 4545, 2016.

851 O'Neill, J. F., Edwards, T. L., Martin, D. F., Shafer, C., Cornford, S. L., Seroussi, H. L., Nowicki, S., Adhikari, M., and
852 Gregoire, L. J.: ISMIP6-based Antarctic projections to 2100: simulations with the BISICLES ice sheet model, *The Cryosphere*,
853 19, 541-563, 2025.

854 Pattyn, F. and Morlighem, M.: The uncertain future of the Antarctic Ice Sheet, *Science*, 367, 1331-1335, 2020.

855 Payne, A. J., Nowicki, S., Abe-Ouchi, A., Agosta, C., Alexander, P., Albrecht, T., Asay-Davis, X., Aschwanden, A., Barthel,
856 A., and Bracegirdle, T. J.: Future sea level change under coupled model intercomparison project phase 5 and phase 6 scenarios
857 from the Greenland and Antarctic ice sheets, *Geophysical Research Letters*, 48, e2020GL091741, 2021.

858 Pollard, D. and DeConto, R.: Description of a hybrid ice sheet-shelf model, and application to Antarctica, *Geoscientific Model
859 Development*, 5, 1273-1295, 2012.

860 Quiquet, A., Dumas, C., Ritz, C., Peyaud, V., and Roche, D. M.: The GRISLI ice sheet model (version 2.0): calibration and
861 validation for multi-millennial changes of the Antarctic ice sheet, *Geoscientific Model Development*, 11, 5003-5025, 2018.
862

863 Reese, R., Garbe, J., Hill, E. A., Urruty, B., Naughten, K. A., Gagliardini, O., Durand, G., Gillet-Chaulet, F., Gudmundsson,
864 G. H., and Chandler, D.: The stability of present-day Antarctic grounding lines—Part 2: Onset of irreversible retreat of
865 Amundsen Sea glaciers under current climate on centennial timescales cannot be excluded, *The Cryosphere*, 17, 3761-3783,
866 2023.

867 Rignot, E., Mouginot, J., and Scheuchl, B.: Ice flow of the Antarctic ice sheet, *Science*, 333, 1427-1430, 2011.

868 Rignot, E., Jacobs, S., Mouginot, J., and Scheuchl, B.: Ice-shelf melting around Antarctica, *Science*, 341, 266-270, 2013.
869

870 Robel, A. A., Seroussi, H., and Roe, G. H.: Marine ice sheet instability amplifies and skews uncertainty in projections of future
871 sea-level rise, *Proceedings of the National Academy of Sciences*, 116, 14887-14892, 2019.

872 Robinson, A., Goldberg, D., and Lipscomb, W. H.: A comparison of the stability and performance of depth-integrated ice-
873 dynamics solvers, *The Cryosphere*, 16, 689-709, 2022.

874 Rosier, S. H., Gudmundsson, G. H., Jenkins, A., and Naughten, K. A.: Calibrated sea level contribution from the Amundsen
875 Sea sector, West Antarctica, under RCP8. 5 and Paris 2C scenarios [preprint], *EGUsphere*, 2024.

876 Rosier, S. H., Reese, R., Donges, J. F., De Rydt, J., Gudmundsson, G. H., and Winkelmann, R.: The tipping points and early
877 warning indicators for Pine Island Glacier, West Antarctica, *The Cryosphere*, 15, 1501-1516, 2021.

878 Scott, W. I., Kramer, S. C., Holland, P. R., Nicholls, K. W., Siegert, M. J., and Piggott, M. D.: Towards a fully unstructured
879 ocean model for ice shelf cavity environments: Model development and verification using the Firedrake finite element
880 framework, *Ocean Modelling*, 182, 102178, 2023.

881 Seroussi, H.: Insights on the vulnerability of Antarctic glaciers from the ISMIP6 ice sheet model ensemble, AGU Fall Meeting
882 Abstracts, C15C-0818,

883 Seroussi, H. and Morlighem, M.: Representation of basal melting at the grounding line in ice flow models, *The Cryosphere*,
884 12, 3085-3096, 10.5194/tc-12-3085-2018, 2018.

885 Seroussi, H., Nowicki, S., Payne, A. J., Goelzer, H., Lipscomb, W. H., Abe-Ouchi, A., Agosta, C., Albrecht, T., Asay-Davis,
886 X., and Barthel, A.: ISMIP6 Antarctica: a multi-model ensemble of the Antarctic ice sheet evolution over the 21st century,
887 *The Cryosphere*, 14, 3033-3070, 2020.

888 Seroussi, H., Pelle, T., Lipscomb, W. H., Abe-Ouchi, A., Albrecht, T., Alvarez-Solas, J., Asay-Davis, X., Barre, J. B., Berends,
889 C. J., and Bernaldes, J.: Evolution of the Antarctic Ice Sheet over the next three centuries from an ISMIP6 model ensemble,
890 *Earth's Future*, 12, e2024EF004561, 2024.

891 Seroussi, H., Verjans, V., Nowicki, S., Payne, A. J., Goelzer, H., Lipscomb, W. H., Abe Ouchi, A., Agosta, C., Albrecht, T.,
892 and Asay-Davis, X.: Insights on the vulnerability of Antarctic glaciers from the ISMIP6 ice sheet model ensemble and
893 associated uncertainty, *The Cryosphere Discussions*, 2023, 1-28, 2023.

894 Siahaan, A., Smith, R. S., Holland, P. R., Jenkins, A., Gregory, J. M., Lee, V., Mathiot, P., Payne, A. J., Ridley, J. K., and
895 Jones, C. G.: The Antarctic contribution to 21st-century sea-level rise predicted by the UK Earth System Model with an
896 interactive ice sheet, *The Cryosphere*, 16, 4053-4086, 2022.

897 Smith, B., Fricker, H. A., Gardner, A. S., Medley, B., Nilsson, J., Paolo, F. S., Holschuh, N., Adusumilli, S., Brunt, K., and
898 Csatho, B.: Pervasive ice sheet mass loss reflects competing ocean and atmosphere processes, *Science*, 368, 1239-1242, 2020.
899

900 van Calcar, C., Bernaldes, J., Berends, C., van der Wal, W., and van de Wal, R.: Bedrock uplift reduces Antarctic sea-level
901 contribution over next centuries, 2024.

902 van de Wal, R. S., Nicholls, R. J., Behar, D., McInnes, K., Stammer, D., Lowe, J. A., Church, J. A., DeConto, R., Fettweis,
903 X., and Goelzer, H.: A High-End Estimate of Sea Level Rise for Practitioners, *Earth's future*, 10, e2022EF002751, 2022.
904

905 van den Akker, T., Lipscomb, W. H., Leguy, G. R., van de Berg, W. J., and van de Wal, R. S. W.: Competing processes
906 determine the long-term impact of basal friction parameterizations for Antarctic mass loss, *EGUosphere*, 2025, 1-35,
907 10.5194/egusphere-2025-441, 2025a.

908 van den Akker, T., Lipscomb, W. H., Leguy, G. R., Bernaldes, J., Berends, C. J., van de Berg, W. J., and van de Wal, R. S.:
909 Present-day mass loss rates are a precursor for West Antarctic Ice Sheet collapse, *The Cryosphere*, 19, 283-301, 2025b.
910

911 Van Wessem, J. M., Van De Berg, W. J., Noël, B. P., Van Meijgaard, E., Amory, C., Birnbaum, G., Jakobs, C. L., Krüger, K.,
912 Lenaerts, J. T., and Lhermitte, S.: Modelling the climate and surface mass balance of polar ice sheets using RACMO2–Part 2:
913 Antarctica (1979–2016), *The Cryosphere*, 12, 1479-1498, 2018.

914 Wilner, J. A., Morlighem, M., and Cheng, G.: Evaluation of four calving laws for Antarctic ice shelves, *The Cryosphere*
915 *Discussions*, 2023, 1-19, 2023.

916 Winkelmann, R., Martin, M. A., Haseloff, M., Albrecht, T., Bueller, E., Khroulev, C., and Levermann, A.: The Potsdam parallel
917 ice sheet model (PISM-PIK)–Part 1: Model description, *The Cryosphere*, 5, 715-726, 2011.

918 Yu, H., Rignot, E., Seroussi, H., Morlighem, M., and Choi, Y.: Impact of iceberg calving on the retreat of Thwaites Glacier,
919 West Antarctica over the next century with different calving laws and ocean thermal forcing, *Geophysical Research Letters*,
920 46, 14539-14547, 2019.

921 Zoet, L. K. and Iverson, N. R.: A slip law for glaciers on deformable beds, *Science*, 368, 76-78, 2020.
922
923